Nucleic Acids Research, 2025, **53**, gkaf301
https://doi.org/10.1093/nar/gkaf301
Chemical Biology and Nucleic Acid Chemistry

Naphthalene diimide-naphthalimide dyads promote telomere damage by selectively targeting multimeric G-quadruplexes

Valentina Pirota [1,†], Sara Iachettini [2,†], Chiara Platella [3,†], Pasquale Zizza [2,*], Giorgia Fracchioni [1], Serena Di Vito [2], Alice Carachino [2], Federica Battistini [4,5], Modesto Orozco [4,5], Mauro Freccero [1], Annamaria Biroccio [2,‡], Daniela Montesarchio [3,*,‡], Filippo Doria [1,*,‡]

[1]Department of Chemistry, University of Pavia, 27100 Pavia, Italy
[2]Translational Oncology Research Unit, IRCCS - Regina Elena National Cancer Institute, 00144 Rome, Italy
[3]Department of Chemical Sciences, University of Naples Federico II, 80126 Naples, Italy
[4]Institute for Research in Biomedicine (IRB Barcelona), The Barcelona Institute of Science and Technology, 08028 Barcelona, Spain
[5]Department of Biochemistry and Biomedicine, University of Barcelona, 08028 Barcelona, Spain

[*]To whom correspondence should be addressed. Email: filippo.doria@unipv.it
Correspondence may also be addressed to Daniela Montesarchio. Email: daniela.montesarchio@unina.it
Correspondence may also be addressed to Pasquale Zizza. Email: pasquale.zizza@ifo.it
[†]The first three authors should be regarded as Joint First Authors.
[‡]The last three authors should be regarded as Joint Last Authors.

Abstract

G-quadruplex (G4) nucleic acid ligands have attracted significant attention as putative anticancer agents for selectively stabilizing telomeric structures. In our pursuit of targeting the most biologically relevant telomeric structures, we have investigated a new class of naphthalene diimide (NDI)-based ligands designed to bind multimeric G4s. The NDI unit covalently linked with one 1,8-naphthalimide (NI) moiety, results in ligands able to fold into a sandwich-like conformation fitting into the binding pockets of telomeric multimeric G4s, thus optimizing binding complementarity. Varying the NDI decorations, we synthesized a small library of NDI-NI dyads and then examined their capability of stabilizing G4s by biophysical assays. Given the relevance of G4 stabilizing agents in fighting cancer, the most promising NDI-NIs were evaluated for their antitumoral activity on a panel of human cell lines originating from different tumor histotypes. Obtained results evidenced that three of the selected ligands promoted an accumulation of telomere-localized damage leading to a robust impairment of cell viability, regardless of homologous recombination status. These data, then confirmed in advanced 3D models, paved the way for the advancement of NDI-NIs as a new class of clinically relevant antitumoral agents. Finally, computational analyses gained deeper insight into their binding modality.

Graphical abstract

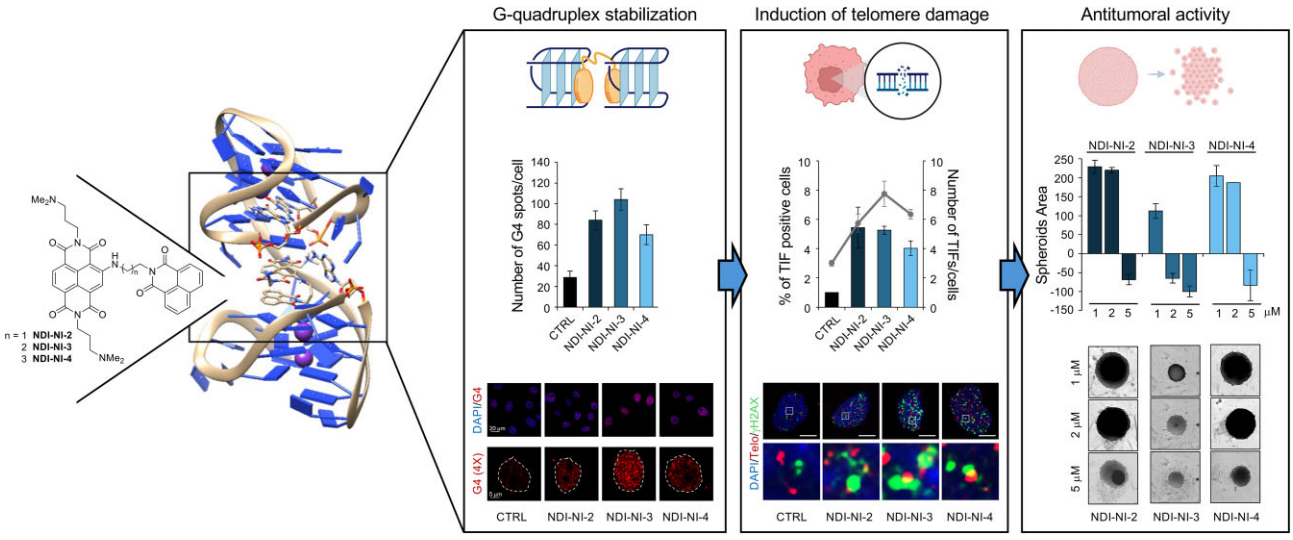

Received: June 17, 2024. **Revised:** March 26, 2025. **Editorial Decision:** March 27, 2025. **Accepted:** April 2, 2025

Introduction

G-quadruplexes (G4s) are high-order non-canonical structures of nucleic acids clustered in crucial genomic regions rich in guanine bases, including telomeres, gene promoters, and recombination sites. They are recognized as pivotal structural elements involved in several biological processes, such as inhibition of telomerase activity, maintenance of telomere homeostasis, and regulation of gene transcription [1]. Therefore, in the last decades, G4s have been recognized as important targets in biomedical research, stimulating researchers to develop countless stabilizing G4 ligands as potential drugs in cancer treatment, in most cases having telomeric DNA G4s as their primary target [2]. Noteworthy, compounds specifically recognizing telomeric G4s exhibit high selectivity for cancer cells. This is due, on one side, to inhibition of the telomerase activity (long-term effect) and, on the other side, to the presence of a basal level of DNA damage, including at the telomere level [3].

Until a few years ago, the prevailing model for G4-forming telomeric DNA, which required huge efforts to optimize high affinity and selectivity binders, was a monomeric G4 structure adopting hybrid conformation in K^+-rich solutions [4–6].

More recently, it has been demonstrated that the single-stranded overhang of telomeric DNA, spanning ∼150–300 nucleotides, can assemble into multimeric G4s [7, 8]. Thus, intense research efforts have been aimed at developing tailored binders with high affinity and selectivity for telomeric multimeric G4s as a more precise strategy to target telomeres [9–12]. Two different structural models have been proposed for the telomeric G4 repeats. The first one consists of adjacent monomeric G4s folding independently, wherein each G4 unit does not interact with the nearby G4s ("beads on a string" model in Fig. 1) [13]. In contrast, the second one is represented by superstructures in which single G4s interact with the neighboring ones via "stacking interfaces," forming peculiar binding pockets (Fig. 1) [14]. Considering the unique, distinctive features of G4 multimers, different ligands have been designed to selectively interact with these targets. In detail, three different types of binding modes for multimeric G4s have been defined thus far: (i) monomeric or dimeric ligands can recognize the target via their monomeric cores, each interacting with a single G4 structure on the "beads on a string" multimeric model (Fig. 1, left); (ii) monomeric ligands can fit in the binding pocket formed between two consecutive G4s in "stacking interfaces" multimers (Fig. 1, middle); and (iii) dimeric ligands can interact with one of their constitutive units at the interface between two consecutive G4s in "stacking interfaces" multimers, while the second unit can externally interact with the grooves or loops of one of the adjacent G4 units (Fig. 1, right) [14].

In this frame, naphthalene diimides (NDIs)-based ligands emerged as promising anticancer drugs due to their strong ability to interact with telomeric multimeric G4s through different binding modes. Their extended aromatic surface allows a tight binding with planar G-quartets driven by stacking interactions. In addition, NDIs are particularly noteworthy for their remarkable binding versatility, largely attributed to their differently modifiable core structure [15]. This feature enables the incorporation of multiple interacting moieties, thus making NDIs a perfect substrate for *ad hoc* tailored design, enhancing their binding specificity and efficacy [15–18].

Specifically, our previous studies highlighted that the monomeric **NDI-5** showed remarkable recognition selectivity for telomeric G4s (monomeric tel26 and dimeric tel46 models) over DNA duplex structure ds27 (selectivity index CPG-tel46/CPG-ds27 = 3.1), with a high binding affinity (K_a ∼ 1.6 × 10^7 M^{-1}, as determined by ITC) and notable stabilization effects (ΔT_m of 12°C observed in CD-melting assays) versus dimeric tel46 model. As emphasized by docking studies, these results arise from its ability to perfectly intercalate between the two consecutive G4 units of tel46, interacting with them simultaneously by stacking interactions (Supplementary Fig. S1) [19, 20]. Biologically, **NDI-5** induced a significant increase in γH2AX, a marker of DNA damage, specifically in transformed fibroblasts (BJ-EHLT), while sparing normal fibroblasts. However, only a portion of this DNA damage was localized at telomere level, suggesting that the mechanism of action of **NDI-5** may extend beyond telomeric targeting [19]. An alternative binding mode was reported for NDI–NDI dimer **1** carrying a long alkyl spacer by Manoli *et al.* [21, 22]. In this model, the trisubstituted NDI unit well fits the binding pocket formed between two consecutive G4s, interacting through stacking interactions, whereas the tetrasubstituted NDI unit sticks out of the pocket and binds one of the adjacent G4 units, exploiting additive binding interactions, i.e. electrostatic and cation-π interactions with the phosphate backbone or nucleotide bases, respectively (Supplementary Fig. S1) [22]. This distinct binding mode enabled the NDI–NDI dimer **1** to achieve a one-order magnitude higher selectivity for the telomeric multimeric G4 model htg45 ($K_{1:1}$ ∼ 1.29 × 10^7 M^{-1}, as determined by fluorescence titration data) over the telomeric monomeric G4 hTel22 [22]. Although the compound effectively triggered DNA damage responses (DDRs) and induced telomere dysfunction with notable selectivity for cancer cells over normal cells, the observed DDR foci were not confined exclusively to telomeres [21]. This result aligns with the limitations posed by the large size and fixed orientation of the NDI–NDI dimer **1** units that constrained the ligand ability to fit seamlessly within the multimeric G4 pocket, thus reducing its selectivity.

Specifically, we hypothesized that dimeric compounds capable of self-folding into a bent conformation, allowing them to well fit into the binding pocket formed by two adjacent G4 units, could bind with optimized affinity and selectivity to telomeric multimeric G4s by forming stable sandwich-like complexes (Fig. 2, left). Therefore, we engineered a new family of hetero-dyads (Fig. 2, right), composed of one NDI and one smaller 1,8-naphthalimide (NI) unit, connected through variable length linkers. Considering that in the case of homodimeric NDIs (like NDI–NDI dimer **1**), the bent conformation was probably prevented by their large cores as well as by the mutual orientations between the two NDI units, we introduced three main structural changes in our novel design. Firstly, one NDI unit was replaced with an NI moiety to reduce size and steric hindrance. Secondly, the mutual orientation between the two aromatic units was changed by connecting the NDI core directly to the imide position of the NI. Lastly, the number of side chains was reduced to decrease the steric hindrance within the binding pocket.

Thus, we synthesized seven different NDI-NI hetero-dyads featuring alkyl linkers of different lengths, keeping their constitutive units close to each other but flexible enough to enable them to freely interact (NDI-NI-n, Fig. 2). The first group of four dyads retains the trisubstituted NDI core, as for the

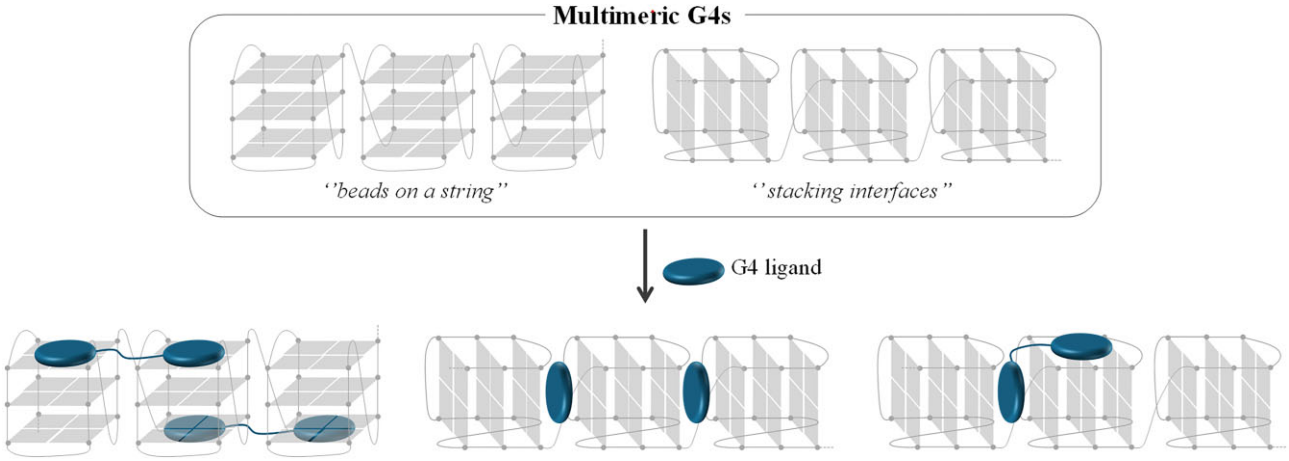

Figure 1. Binding mode on multimeric G4s. Cartoon representation of telomeric multimeric G4 structures and potential binding modes of ligands thereof.

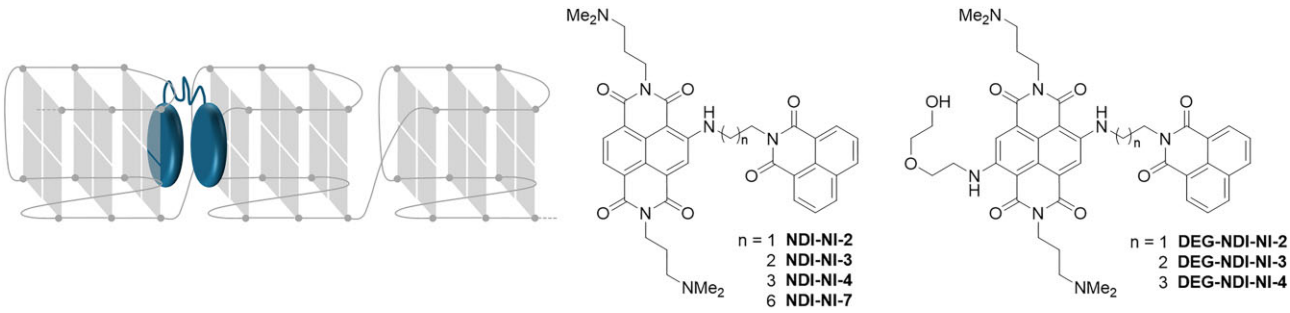

Figure 2. New NDI-NIs compounds. Representative cartoon of the putative interactions of the here investigated NDI-NIs hetero-dyads with a multimeric telomeric G4 model (left) and NDI-NIs chemical structures (right).

NDI–NDI dimer **1**, since it is considered the best ligand for the multimeric telomeric G4 binding pocket according to the work of Manoli *et al.* [22]. Differently, the second group of three NDI-NIs featured by a tetrasubstituted NDI unit carrying a 2-(2-aminoethoxy)ethanol side-chain (DEG), considering its fundamental contribution in the selective binding of **NDI-5** to the telomeric dimeric G4 model tel46 (DEG-NDI-NI-n, Fig. 2) [19].

This library of brand new NDI-NI hetero-dyads has been evaluated in detail by biophysical studies as free species and in their interaction with the telomeric dimeric G4 tel46, together with the telomeric monomeric G4 tel26 and a duplex structure (ds12) as proper controls. Subsequently, all the synthesized ligands have been tested for their biological activity to assess their potential as anticancer agents as well as their ability to target telomeric DNA selectively. The behavior of the most promising compounds was validated in advanced 3D models that recapitulate, *in vitro*, the architectural complexity of tumors. Finally, computational studies have confirmed their folding and binding mode to the telomeric dimeric G4 model tel46.

Materials and methods

Chemistry

Reagents, solvents, and chemicals were used as supplied from commercial sources (Alfa Aesar, Sigma–Aldrich, TCI, or Fluorochem) without further purification. TLC analyses were carried out on silica gel (Merck 60F-254) with visualization at 254 and 366 nm. For flash column chromatography purification, Isolera ONE® Flash Chromatography System (MPLC, Biotage), combined with a tunable wavelength UV/vis detector, was used (SNAP KP-SIL 25 or 50 g columns, Biotage). All the syntheses assisted by microwaves were performed using a Discover microwave synthesizer (CEM). HPLC analyses were performed using an Agilent system SERIES 1260 with a SepaChrom ROBUSTA C18 column (3 μm, 4.6 × 50 mm) column and a flow rate of 1.4 ml/min. The following method was used: isocratic elution over 2 min at 95% of 0.1% trifluoroacetic acid in water/5% acetonitrile, gradually increasing to 60% acetonitrile over 8 min, and then isocratic elution for 4 min ($\lambda = 256$ nm). Compounds were purified on an Agilent Technologies 1260 Infinity preparative HPLC, by using a Waters XSelect® CSH Prep C18 OBDTM (5 μm, 100 × 30 mm), with a flow of 30 ml/min. The following method was used: isocratic elution over 2 min at 95% of 0.1% trifluoroacetic acid in water/5% acetonitrile, gradually increasing to 40% acetonitrile over 16 min, and then isocratic elution for 8 min ($\lambda = 256, 550, 600$ nm). ^{1}H- and ^{13}C-NMR spectra were recorded on a Bruker ADVANCE 300 MHz spectrometer. High-resolution mass spectra (HRMS) were recorded on an X500B QTOF System (AB Sciex) with an ESI ion source. HPLC purity analysis, UHPLC-HRMS chromatograms, as well as NMR spectra of the compound here studied are reported in the supporting information.

The oligonucleotides d[AGGG(TTAGGG)$_7$] (tel46), d(TTAGGGTTAGGGTTAGGGTTAGGGTT) (tel26) and d(CGCGAATTCGCG) (ds12) were purchased as HPLC-purified compounds with a purity >99% from Biomers.

Synthesis of the NI units

Four equivalents of the proper amine were added to a solution of commercial 1,8-naphthalic anhydride (1.01 mmol, 0.200 g) in ethanol (60 ml), and the reaction mixture was refluxed under argon for 2 h. In detail, 4 equiv. of 1,2-diaminoethane (4.04 mmol, 270 µl) for **NI-2**, of 1,3-diaminopropane (4.04 mmol, 340 µl) for **NI-3**, of 1,4-diaminobutane (4.04 mmol, 406 µl) for **NI-4**, and of 1,7-diaminoheptane (4.04 mmol, 526 µl) for **NI-7** were used. After 2 h, the solvent was removed under reduced pressure obtaining a solid that was then dissolved in 50 ml of a saturated sodium bicarbonate aqueous solution and extracted with CH_2Cl_2 (3 × 30 ml). The organic layers were dried over anhydrous sodium sulfate and then evaporated. The resulting solid was washed with ethanol, methanol, and diethyl ether to remove the excess of amine. **NI-4** and **NI-7** were obtained as pale-yellow solids with yields of 50% (155 mg) and 88% (286.4 mg), respectively, and a high purity degree. A purification step on Isolera ONE® system was performed to obtain pure **NI-2** and **NI-3** (TLC eluting system: CH_2Cl_2:CH_3OH with 0.1% Et_3N = 8:2, $R_{f\ NI\text{-}2}$: 0.51, $R_{f\ NI\text{-}3}$: 0.58), with yields of 52% (125 mg) and 43% (136 mg), respectively. The compound purity was evaluated by analytical HPLC. The compliance of **NI-2**, **NI-3**, and **NI-4** structures with literature data was confirmed by ^{1}H-NMR analysis. [23] **NI-7** was characterized by NMR. For all the synthesized NIs, UHPLC-HRMS analyses were performed to further confirm the identity of the final products.

NI-2. Yield = 52%. Analytical HPLC retention time: 5.27 min (97.5%).

UHPLC-HRMS (positive mode): 241.0975 *m/z*; precursor mass: 241.0972 *m/z*. ^{1}H-NMR (200 MHz, D_2O): δ ppm: 8.52 (2H, d, J = 7.3 Hz), 8.33 (2H, d, J = 8.1 Hz), 7.83–7.77 (2H, m), 4.37 (2H, t, J = 6.0 Hz), 3.18 (2H, s).

NI-3. Yield = 43%. Analytical HPLC retention time: 5.62 min (95.0%).

UHPLC-HRMS (positive mode): 255.1132 *m/z*; precursor mass: 255.1128 *m/z*. ^{1}H-NMR (200 MHz, $CDCl_3$): δ ppm: 8.56 (2H, d, J = 7.0 Hz), 8.19 (2H, d, J = 8.0), 7.76–7.69 (2H, m), 4.26 (2H, t, J = 6.6 Hz), 2.75 (2H, t, J = 6.2 Hz), 1.92–1.84 (2H, m).

NI-4. Yield = 50%. Analytical HPLC retention time: 5.86 min (97.7%).

UHPLC-HRMS (positive mode): 269.1289 *m/z*; precursor mass: 269.1285 *m/z*. ^{1}H-NMR (200 MHz, $CDCl_3$): δ ppm: 8.57 (2H, d, J = 7.3 Hz), 8.19 (2H, d, J = 8.2), 7.77–7.69 (2H, m), 4.22–4.15 (2H, m), 2.83–2.76 (2H, m), 1.72 (4H, m).

NI-7. Yield = 88%. Analytical HPLC retention time: 6.75 min (91.0%).

UHPLC-HRMS (positive mode): 311.1759 *m/z*; precursor mass: 311.1754 *m/z*. ^{1}H-NMR (300 MHz, $CDCl_3$) δ ppm: 8.58 (2H, d, J = 7.3 Hz), 8.19 (2H, d, J = 8.2 Hz), 7.76–7.71 (2H, m), 4.17 (2H, t, J = 7.5 Hz), 2.70–2.65 (2H, m), 1.74 (4H, m), 1.42 (6H, m). ^{13}C-NMR (75.4 MHz, $CDCl_3$) δ ppm: 164.0, 133.7, 131.4, 131.0, 128.0, 126.8, 122.6, 42.0, 40.3, 33.4, 29.0, 27.9, 26.9, 26.6.

Synthesis of NDI-NIs and DEG-NDI-NIs

50 mg of pure **Br_2-NDI** (0.084 mmol) synthesized as previously reported [24], were dissolved in 50 ml of CH_3CN. Subsequently, 2.5 equiv. of the suitable NI were added (**NI-2**: 0.212 mmol, 51 mg; **NI-3**: 0.211 mmol, 54 mg; **NI-4**: 0.211 mmol, 57 mg; **NI-7**: 0.211 mmol, 65.5 mg) and the resulting mixture were stirred at reflux for 16 h under argon. The crude products were dried under vacuum, then treated with a 10% HCl solution (*v/v*) until reaching, pH 4–5 and extracted with CH_2Cl_2 (3 × 50 ml). The organic phases were collected, dried over anhydrous sodium sulfate, and concentrated under vacuum. The crudes were resuspended in the minimum volume of 2-(2-aminoethoxy)ethanol (DEG) and stirred for 10 min at 120°C under microwave assistance. The solvent was evaporated under vacuum, and the mixtures were purified by preparative HPLC. The final purity of each compound was evaluated through analytical HPLC. All the isolated compounds were characterized by UHPLC-HRMS and NMR (300 MHz) analyses.

NDI-NI2. Yield = 92%. Analytical HPLC retention time: 5.07 min (99.4%).

UHPLC-HRMS (positive mode): 675.2937 *m/z*; precursor mass: 675.2926 *m/z*. ^{1}H-NMR (300 MHz, D_2O, 60°C) δ ppm: 8.17 (1H, bs), 7.99–7.92 (3H, m), 7.72–7.69 (1H, m), 7.58–7.53 (2H, m), 7.22–7.17 (2H, m), 4.24–4.19 (6H, m), 3.82–3.78 (2H, m), 3.66–3.55 (4H, m), 3.32 (6H, s), 3.38 (6H, s), 2.41–2.35 (4H, m). ^{13}C-NMR (75.4 MHz, D_2O, 60°C) δ ppm: 164.6, 164.0, 163.1, 162.9, 161.9, 161.4, 152.5, 134.8, 131.4, 130.5, 130.3, 129.9, 127.4, 126.5, 126.4, 125.7, 124.5, 124.0, 121.4, 119.3, 117.2, 98.8, 55.5, 43.2, 39.6, 39.0, 38.1, 37.4, 22.9.

NDI-NI3. Yield = 88%. Analytical HPLC retention time: 5.48 min (97.3%).

UHPLC-HRMS (positive mode): 688.3096 *m/z*; precursor mass: 688.3082 *m/z*. ^{1}H-NMR (300 MHz, D_2O) δ ppm: 7.73–7.71 (1H, m), 7.58–7.52 (3H, m), 7.41–7.33 (2H, m), 7.29 (1H, s), 7.02 (2H, t, J = 7.65), 3.91–3.88 (2H, m), 3.84–3.79 (2H, m), 3.71–3.67 (2H, m), 3.36–3.33 (2H, bs), 3.24–3.10 (4H, m), 2.89–2.81 (12H, m), 2.07–1.94 (6H, m). ^{13}C-NMR (75.4 MHz, D_2O) δ ppm: 164.4, 164.0, 163.1, 162.8, 162.3, 151.1, 134.4, 130.8, 130.4, 129.8, 127.1, 126.6, 125.9, 125.5, 124.4, 124.3, 121.1, 119.5, 117.2, 97.8, 55.1, 42.7, 40.9, 38.2, 37.6, 36.9, 36.9, 26.0, 22.6.

NDI-NI4. Yield = 89%. Analytical HPLC retention time: 5.57 min (98.4%).

UHPLC-HRMS (positive mode): 703.3253 *m/z*; precursor mass: 703.3239 *m/z*. ^{1}H-NMR (300 MHz, D_2O) δ ppm: 7.71–7.67 (1H, m), 7.54–7.42 (3H, m), 7.32–7.29 (2H, m), 7.14 (1H, s), 6.96 (2H, t, J = 7.28), 3.87–3.79 (4H, m), 3.60–3.57 (2H, m), 3.23–3.12 (6H, m), 2.90 (12H, s), 2.01–1.98 (4H, m), 1.58 (4H, bs). ^{13}C-NMR (75.4 MHz, D_2O) δ ppm: 164.3, 163.9, 163.0, 162.7, 162.1, 150.6, 134.4, 130.9, 130.1, 129.7, 127.2, 126.3, 125.5, 125.4, 124.2, 124.1, 121.2, 119.5, 119.0, 116.8, 97.7, 55.1, 55.0, 42.7, 41.6, 39.8, 37.6, 37.0, 24.9, 23.5, 22.7.

NDI-NI7. Yield = 82%. Analytical HPLC retention time: 7.72 min (99.5%).

UHPLC-HRMS (positive mode): 745.3699 *m/z*; precursor mass: 745.3708 *m/z*. ^{1}H-NMR (300 MHz, D_2O) δ ppm: 7.85–7.82 (2H, m), 7.67–7.64 (1H, m), 7.45–7.41 (1H, m), 7.37–7.33 (2H, m), 7.26 (1H, s), 7.01 (2H, t, J = 7.0), 3.89–3.86 (4H, m), 3.58–3.55 (2H, m), 3.26–3.23 (6H, m), 2.93 (6H, s), 2.91 (6H, s), 2.07–1.88 (4H, m), 1.74–1.70 (2H, m), 1.58–1.24 (8H, m). ^{13}C-NMR (75.4 MHz, D_2O) δ ppm: 164.6, 163.7, 163.0, 162.8, 162.3, 151.1, 134.6, 130.3, 129.9, 127.4, 126.7, 126.2, 125.8, 125.5, 124.1, 123.9, 121.0, 120.2, 119.7, 119.5, 117.1, 97.4, 55.2, 55.1, 42.7, 40.2, 39.4, 37.6, 28.3, 28.1, 27.7, 27.5, 26.5, 26.2, 25.9, 25.4, 22.7.

DEG-NDI-NI2. Yield = 32%. Analytical HPLC retention time: 6.47 min (100%).

UHPLC-HRMS (positive mode): 778.3557 *m/z*; precursor mass: 777.3486 *m/z*. ^{1}H-NMR (300 MHz, D_2O, 60°C) δ ppm: 8.24–7.96 (4H, m), 7.84 (1H, bs), 7.64–7.33 (3H, m), 4.52–4.06 (12H, m), 3.88 (4H, bs), 3.80–3.60 (4H, m), 3.50–3.31 (12H, m), 2.59–2.39 (4H, m).

DEG-NDI-NI3. Yield = 23%. Analytical HPLC retention time: 6.60 min (94.8%).

UHPLC-HRMS (positive mode): 792.6064 *m/z*; precursor mass: 792.3643 *m/z*. ^{1}H-NMR (300 MHz, D_2O, 60°C) δ ppm: 7.71 (4H, bs), 7.36–7.27 (4H, m), 4.33–3.82 (12H, m), 3.70–3.44 (8H, m), 3.28 (12H, bs), 2.32 (4H, bs), 2.09 (2H, bs). ^{13}C-NMR (75.4 MHz, D_2O, 60°C) δ ppm: 164.9, 164.7, 164.0, 163.0, 162.7, 162.5, 148.2, 134.5, 130.5, 126.7, 125.8, 123.8, 122.7, 119.7, 119.4, 118.7, 118.0, 114.8, 100.6, 98.0, 72.3, 69.1, 61.0, 55.6, 54.8, 43.2, 42.3, 38.6, 37.4, 26.5, 23.1.

DEG-NDI-NI4. Yield = 28%. Analytical HPLC retention time: 6.06 min (95.1%).

UHPLC-HRMS (positive mode): 806.3879 *m/z*; precursor mass: 806.3872 *m/z*. ^{1}H-NMR (300 MHz, D_2O, 60°C) δ ppm: 7.98 (2H, bs), 7.88 (2H, bs), 7.58–7.40 (4H, m), 4.25–4.06 (10H, m), 3.89 (2H, bs), 3.68–3.47 (8H, m), 3.34 (12H, bs), 2.42 (4H, bs), 2.00 (2H, bs). ^{13}C-NMR (75.4 MHz, D_2O, 60°C) δ ppm: 164.8, 164.7, 164.0, 163.0, 162.7, 162.4, 148.5, 147.8, 134.5, 130.5, 130.3, 126.6, 123.9, 123.5, 120.5, 118.7, 117.7, 114.8, 100.4, 99.7, 72.3, 69.2, 61.0, 55.7, 47.2, 43.3, 42.4, 41.6, 40.3, 37.7, 36.7, 24.7, 23.3, 23.1.

Spectroscopic and spectrofluorimetric analyses of hetero-dyads alone

Spectroscopic studies were performed on an Agilent Cary 60 spectrophotometer equipped with a Cary Single Cell Peltier temperature controller. The spectra were recorded at 25°C in a quartz cuvette with a 1 cm optical length in the 200–800 nm wavelength range with a scan rate of 100 nm/min and a slits width of 1 nm. In MilliQ water, NDI-NIs and DEG-NDI-NIs were dissolved to a final stock concentration of 1 mM. Their aggregation propensity was then investigated by UV-vis analysis carried out at increasing concentrations (from 1 to 20 μM) in five different solutions: MeOH; MilliQ water; MilliQ water with 10 mM SDS; 5 mM potassium phosphate buffer pH 7.0; and 5 mM potassium phosphate buffer pH 7.0 with 150 mM KCl.

Emission experiments were run on an Agilent Cary Eclipse fluorescence spectrophotometer equipped with a Cary Single Cell (1 cm path length) Peltier temperature controller. The fluorescence responses of the hetero-dyads alone dissolved at 4–6–8 μM in MeOH and 6 μM in 5 mM potassium phosphate buffer pH 7.0 with 150 mM KCl were recorded exciting the solutions at wavelengths at which they exhibited comparable absorbance and vibrational state (see below). Fluorescence spectra were recorded with a 600 nm/min scan rate, an averaging time of 0.1 s, and 1 nm of data interval. Slits of 5 nm, excitation filter auto, emission filter open, and a PMT (photomultiplier tube) of 800 V.

Spectroscopic and spectrofluorimetric studies of hetero-dyads interactions with oligonucleotides

The three oligonucleotides tel46, tel26, and ds12 were purchased with an HPLC grade of purity from Biomers.net. 1.5 mM stock solutions of these oligonucleotides were prepared in 5 mM KH_2PO_4 buffer (pH 7.0) with 150 mM of KCl, and annealed by heating them at 95°C for 5 min followed by slowly cooling down to room temperature over 4 h. Stock solutions were frozen and stored at −20°C.

To verify how the interaction with G4s affects NDI-NIs and DEG-NDI-NIs absorption spectra, 5 μM of NDI-NIs and DEG-NDI-NIs (from the previously prepared 1 mM stock solutions) were added to a 1.5 ml solution containing 5 μM of oligonucleotides in 5 mM KH_2PO_4 buffer (pH 7) and 150 mM of KCl. All the solutions were left to equilibrate at r.t. for 4 h and then analyzed by recording UV-vis spectra and fluorescence spectra at 25°C in a 1 cm path length cuvette.

Emission experiments were run on an Agilent Cary Eclipse fluorescence spectrophotometer equipped with a microplate reader (96 wells) or a Cary Single Cell (1 cm path length) Peltier temperature controller. For both the experiments, 5 μM of NDI-NIs or DEG-NDI-NIs (from the previously prepared 1 mM stock solutions) were added to solutions containing 5 mM KH_2PO_4 buffer (pH 7), 150 mM of KCl, and varying concentrations of oligonucleotides (from 0 to 75 μM). All the solutions were left to equilibrate at r.t. for 4 h and then analyzed by recording fluorescence spectra at 25°C (total volumes of solutions: 120 μl for 96-wells plate, 1.5 ml for 1 cm path length cuvette). Fluorescence spectra were recorded with a 600 nm/min scan rate, an averaging time of 0.1 s, and 1 nm of data interval. For the microplate reader, slits of 5 nm were used, with Ex/Em filters open and a PMT of 900 V. For a 1 cm path length cuvette, slits of 10 nm were used, with excitation filter auto, emission filter open, and a PMT of 800 V in the presence of tel46 and tel26 and of 600 V in the presence of ds12. Each spectrum was obtained as the average of three consecutive scans. Data were processed by BindFit v0.5 online software considering a 1:1 interaction [25].

CD analysis

CD spectra were recorded in a quartz cuvette with a path length of 1 cm, on a Jasco J-1500 spectropolarimeter equipped with a Peltier-type temperature control system. The spectra were recorded at 20°C in the range 220–800 nm, with 2 s response, 200 nm/min scanning speed, and 2.0 nm bandwidth, and were corrected by subtraction of the background scan with buffer. All the spectra were averaged over 3 scans. The oligonucleotides were dissolved in a 20 mM KCl, 5 mM KH_2PO_4 buffer (pH 7), thus obtaining 2 μM solutions, which were then annealed by heating them at 95°C for 5 min, followed by slow cooling to r.t. CD titrations were obtained by adding increasing amounts of the ligands (up to 6 molar equiv., corresponding to a 12 μM solution in ligand) to the oligonucleotide solutions. For the CD-melting experiments, the ellipticity versus temperature was monitored at 291 nm for tel46, 289 nm for tel26, and 253 nm for ds12 with a temperature scan rate of 1°C/min, in the range 10–105°C. For the CD-monitored experiments to evaluate the ability of the ligands to induce G4 structuring, 2 μM solutions of tel46 and tel26 were annealed in 10 mM Tris–HCl buffer (pH 7) and then treated with 6 molar equiv. of each ligand.

Cells and culture condition

Human fibroblasts (BJ) and human cervical cancer cells (HeLa) were purchased from American Type Culture Collection (ATCC). BJ-hTERT cells were obtained infecting primary BJ cells with a retrovirus carrying hTERT (Addgene plasmid

#1773); BJ-EHLT derived from the transformation of BJ fibroblasts with hTERT and SV40 early region [26]. Human cervical (HeLa), colorectal (HT29 and HCT116), bone (U2OS and MG63), and breast (MDA-MB-231 and MDA-MB-436) were purchased from ATCC and authenticated. HCT116 TP53$^{-/-}$ were obtained by Dr Vogelstein, Johns Hopkins University, and HCT116 BRCA2$^{-/-}$ were kindly gifted from Dr Madalena Tarsounas. [27] All the mentioned cells were grown in Dulbecco Modified Eagle Medium (DMEM; EuroClone, Milan, Italy, ECM0728L)—supplemented with 10% fetal bovine serum (ThermoFisher Scientific/Gibco, Waltham, MA, USA, 10270–106), 2 mM l-glutamine and antibiotics—at 37°C, in a 5% CO_2-95% air atmosphere.

The NDI-NIs and DEG-NDI-NIs tested in cells were dissolved in DMSO at a concentration of 4 mM, while PDS (Selleckchem, S7444) and RHPS4 (Selleckchem, S8118) were dissolved in DMSO at a concentration of 1.4 and 10 mM, respectively. All the compounds were freshly diluted in DMEM before administration to cells.

Viability assay (crystal violet)

BJ-EHLT and BJ-hTERT were seeded in 24-well plates at a density of 6×10^3 and 1.2×10^4 per well, respectively; HeLa and HT29 at a density of 8×10^3 and 2.2×10^4, respectively; U2OS and MG63 at 1×10^4 and 1.2×10^4; MDA-MB-231 and MDA-MB-436 at 1.2×10^4 and 1.5×10^4, respectively; finally, HCT116 WT, TP53$^{-/-}$, and BRCA2$^{-/-}$ at a density of 2×10^4, 2.5×10^4, and 3×10^4, respectively. After 24 h, cells were treated with the indicated compounds at a final concentration of 0.1, 0.5, 1, and 2 μM for 48 h and then processed for crystal violet staining as previously reported [20].

Immunofluorescence

Cells were grown on glass coverslips, treated for 24 h with the indicated compound at a final concentration of 0.5 μM and processed for IF as previously reported [20].

Briefly, cells were fixed in 3.7% formaldehyde for 15 min, permeabilized with 0.25% Triton X-100 for 5 min, then blocked for 45 min in 3% BSA - 0.1% Tween-20 and incubated with mouse mAb anti-DNA/RNA G-quadruplex structures (BG4 antibody; Absolute Antibody, Oxford, UK, #Ab00174-1.1). After 2 h incubation, cells were washed three times with 0.3% BSA - 0.1% Tween-20 and incubated with anti-mouse IgG (H + L), F (ab')2 Fragment (Alexa Fluor 555 Conjugate; Cell Signaling Technology, Danvers, MA, USA, #4409S) for 1 h. Nuclei were stained with 4′,6-diamidino-2-phenylindole (DAPI; Sigma–Aldrich, D9542), and fluorescence signals were recorded by using a Zeiss Laser Scanning Microscope 510 Meta (63× magnification) (Zeiss, Germany).

FISH combined immunofluorescence

In order to evaluate the DNA damage, immunofluorescence experiments were combined with telomeric fluorescence *in situ* hybridization (FISH) assays as reported by Iachettini *et al.* [28]. Briefly, cells were grown on glass coverslips, treated for 24 h and processed for IF using the mouse mAb anti-phospho-histone H2AX (γH2AX; Millipore, Burlington, Massachusetts, USA, 05–636) as primary antibody and the anti-mouse IgG (H + L), F (ab')2 Fragment (Alexa Fluor 488 Conjugate, Cell Signaling Technology, Danvers, Massachusetts, USA, #4408) as secondary antibody. Successively, cells were subjected to a Telomere specific DNA FISH and the nuclei were stained with DAPI. For quantitative analysis of γH2AX positivity, at least 250 cells/condition were scored in triplicate, while for telomere-induced foci (TIF) analysis, at least 25 γH2AX-positive cells on a single plane were scored. Cells with at least four telomere-γH2AX colocalization spots were considered TIF-positive. Fluorescence signals were recorded with Zeiss Laser Scanning Microscope 510 Meta (63X magnification) (Zeiss, Germany).

Tumor spheroids

Generation and growth analysis

Advanced 3D spheroids were established from human colorectal cancer cells (HCT116) by growing 3×10^3 cells within a drop (20 μl) of a methylcellulose scaffold matrix (day 0). After 2 days of culture (day 2), the spheres were treated with the indicated compound at final concentrations of 1, 2, and 5 μM by adding 10 μl of DMEM containing the compound to each drop. Time course analysis of tumor spheroids growth was monitored by Incucyte® S3 Live-Cell Analysis System (Essen BioScience, Ann Arbor, MI), 10× magnification. The results were expressed as the percentage of the spheroids area upon treatment relative to their own area before the compound administration.

Immunohistochemistry

Spheroids preparation for histological and immunohistochemical staining was performed by a standard protocol for the production of cell blocks. Approximately 0.5 ml of plasma and 0.25–0.5 ml of thrombin were added to the spheroids collected in a tube. By gently shaking, a clot was formed within a few minutes and it was gently transferred to a biopsy cassette, then stored in 10% buffered formalin until further sample processing. Immunohistochemical staining was carried out as reported by Iachettini *et al.* [28]. Sections were immunostained with mouse anti-Ki67 (Dako Omnis, Santa Clara, CA, USA, MIB-1, 1:100), rabbit anti-Cleaved Caspase-3 (Cell Signaling, #9661, 1:100), and rabbit anti-γH2AX (AbCam, Cambridge, UK, EP854 [2]Y, 1:500). Immunostaining results were recorded as percentage of positive cells.

Molecular docking

The tel45 dimeric G4 structure obtained through molecular dynamics (MDs) simulations by Hu *et al.* [12] was used as the target. In parallel, the NMR deposited structure of the tel26 monomeric G4 (PDB 2JPZ) and the ds12 B-DNA duplex (PDB 1NAJ) were used as controls [29]. Molecular docking calculations were carried out using AutoDock Vina with the aid of its graphical user interface AutoDockTools [30]. The ligand and DNA oligonucleotides were prepared by use of AutoDockTools and UCSF Chimera by assigning bond orders, adding hydrogen atoms, and generating the appropriate protonation states. The ligand and DNA oligonucleotides were then converted to proper Autodock PDBQT file formats and the Gaisteiger charges were assigned. The number of torsions was set as the total number of rotatable bonds in each ligand, and specifically TORSDOF = 12, 13, 14, 17 for **NDI-NI-2**, **NDI-NI-3**, **NDI-NI-4**, and **NDI-NI-7**, while TORSDOF = 19, 20, 21 for **DEG-NDI-NI-2**, **DEG-NDI-NI-3**, and **DEG-NDI-NI-4**. The 3D grid box dimensions were defined including the whole DNA macromolecules. The docking area was centered on the DNA center of mass and grid boxes of 118 Å × 92 Å × 70 Å, 92 Å × 80 Å × 60 Å, and 64 Å × 110 Å × 56

Å for tel45 G4, tel26 G4, and ds12 duplex, respectively, with a 0.375 Å spacing, were used. One hundred docking poses were generated by using as docking parameters seed = random, exhaustiveness = 24, and number of binding modes = 20 for each of the five runs performed for each DNA/ligand system. Docking poses were clustered on the basis of their root-mean square deviation and ranked on the basis of their binding energy. Molecular modeling figures were drawn by UCSF Chimera.

MDs simulations

MD simulations were performed starting from the docking structure of the tel45 dimeric G4, including four coordinated K^+ ions, in the presence or absence of the ligand **NDI-NI-3**. The systems were solvated in a truncated octahedral box using the TIP4PEw water model [31], with water molecules extending 10 Å from the complex, and K^+ ions were added to neutralize the net charge. Then, K^+ and Cl^- ions were added at a physiological concentration of 150 mM. The systems were optimized using standard procedures involving energy minimizations, thermalization and a final re-equilibration for 10 ns [32–34], before performing the 1 μs MD simulations. Trajectories were collected in the isothermal-isobaric ensemble ($T = 298$ K, $P = 1$ atm) using the parmbsc1 force field [35] for the tel45 dimeric G4, GAFF parameters [36] for **NDI-NI-3**, and Joung and Cheatham parameters [37] for K^+ and Cl^- ions. Parameters and topology files for the ligand were prepared using Acpype [38, 39]. Simulations were performed using Amber18 [40]. All trajectories were processed using the CPPTRAJ module of the AmberTools18 package using default values. Root mean square deviation values were calculated in each simulation for all the non-hydrogen atoms. MD simulations figures were drawn with the aid of VMD and UCSF Chimera.

Results and discussion

Synthesis of the NDI-NI hetero-dyads

A mini-library of seven NDI-NI derivatives has been prepared according to the synthetic protocols outlined in Fig. 3. In the first step (step a, Fig. 3), the NI units were prepared through a simple and efficient imidation reaction between commercially available 1,8-naphthalic anhydride and the suitable diamine [23]. The dibromo-substituted *N*,*N*'-bis ((dimethylamino)propylamino) NDI (**Br_2-NDI**), used for step b, was synthesized using a well-established method [24] and exploited for the nucleophilic aromatic substitution (S_NAr) in the presence of an excess (2.5 equiv.) of the selected NI-amine (step b, Fig. 3). This process led to partial dehalogenation of the naphthalene core, thus obtaining a mixture of NDI-NI-n and Br-NDI-NI-n, where n indicates the number of methylene groups linking the NDI and NI units. The obtained crudes were used without further purification for the second harsher microwave-assisted S_NAr (step c, Fig. 3) in neat 2-(2-aminoethoxy)ethanol (DEG) carried out in sealed reaction vessels. The reaction occurred in quantitative yield only on the Br-NDI-NI-n substrates. A final HPLC purification step allowed obtaining the desired trisubstituted NDI-NIs and the tetrasubstituted DEG-NDI-NIs hetero-dyads with high yields.

Evaluation of NDI-NI hetero-dyads aggregation behavior

The self-aggregation propensity of the new hetero-dyads in the micromolar concentration range (from 1 to 20 μM) was evaluated by UV-vis studies in different conditions: MeOH; MilliQ water; MilliQ water with 10 mM SDS; 5 mM potassium phosphate buffer pH 7.0; and 5 mM potassium phosphate buffer pH 7.0 with 150 mM KCl. MeOH was chosen as an organic solvent with an intermediate dielectric constant, capable of breaking both intra- and intermolecular π–π interactions between the naphthalene units [41]. In parallel, SDS (sodium dodecyl sulfate), the most widely employed micelle-forming surfactant [42], was exploited to disrupt π–π interactions in aq. solutions. Indeed, NDI-NIs and DEG-NDI-NIs can stack one on top of the other in a bent conformation, strongly intramolecularly interacting in the ground state. Additionally, in the absence of the target, intermolecular interactions between dyads combining identical (NDI_a-NDI_b or NI_a-NI_b) or different (NDI_a-NI_b) units are also possible. In MeOH, all the compounds proved to be disaggregated (Supplementary Fig. S2), showing blue-shifted spectra with a vibronic signature more defined for both the π–π* (300–400 nm) and charge transfer (CT; 450–550 nm) bands and an increase in the total absorbance (Supplementary Fig. S3 and Supplementary Table S1). Conversely, all the spectra recorded in pure water (condition C) or aq. buffers (conditions D and E) were 13–20 nm red-shifted (Supplementary Table S1), with a less defined vibronic signature and a generally decreased absorbance. Nevertheless, reporting the absorbance maxima of the CT bands against NDI-NIs concentrations (Supplementary Fig. S3), the trend was linear ($R^2 > 0.99$; Supplementary Table S1) in this working range, suggesting that the aggregation process was constant and more presumably related to an intramolecular interaction. The π–π* band coalescence underlined the existence of a strong interaction between the NDI and NI units in support of this hypothesis.

The presence of SDS led to contrasting behaviors. **NDI-NI-2** displayed a pronounced red shift with increased absorbance, suggesting micelle-disrupted intermolecular aggregation, strengthening intramolecular interactions (Supplementary Fig. S2). For **NDI-NI-3** and **NDI-NI-4**, no significant changes in CT bands were observed. The spectrum of **NDI-NI-7**, with a longer flexible spacer, showed an enhanced absorbance but not a highly defined shape, suggesting a rearrangement of both intra- and intermolecular interactions. In contrast, DEG-NDI-NIs fully disaggregated under these conditions, akin to their behavior in MeOH.

Taking advantage of the intrinsic fluorescence properties of the NDI core [15], the aggregation behavior of the hetero-dyads was analyzed also based on their fluorescence responses. To ensure comparability, fluorescence spectra were recorded in MeOH (4 μM) and in 5 mM potassium phosphate buffer (pH 7.0) with 150 mM KCl (6 μM) at appropriate wavelengths to achieve equal absorption in both solutions, thereby ensuring an equivalent number of absorbed photons and comparable vibrational states (Supplementary Fig. S4). In MeOH, all the compounds exhibited strong fluorescence, highlighting their bright emissive properties in the disaggregated state. Conversely, in the aq. buffer, distinct behaviors were observed: the emission spectra of NDI-NIs were less intense and red-shifted by ∼20 nm, indicating altered photophysical interactions. Meanwhile, the fluorescence of DEG-NDI-NIs

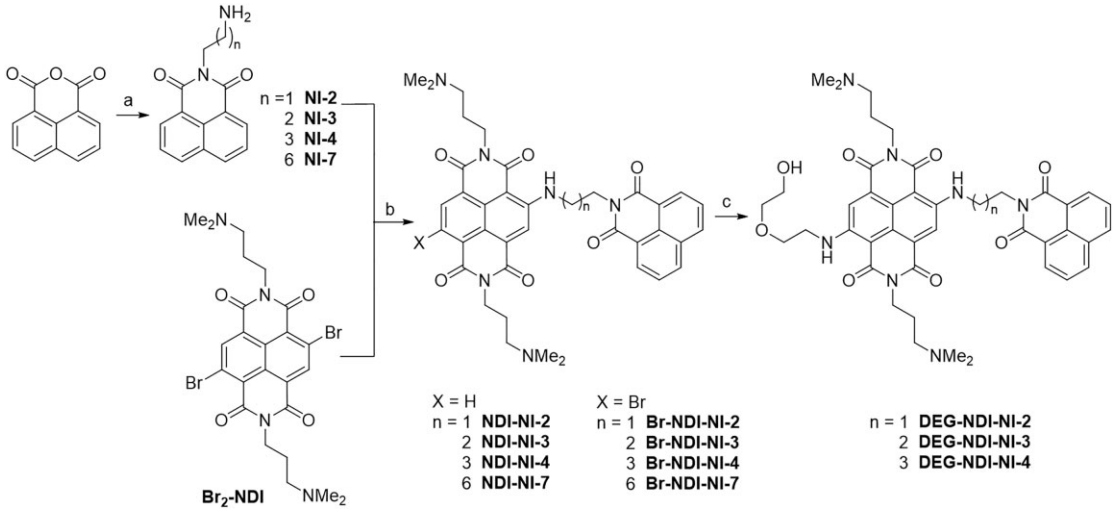

Figure 3. Synthesis of the NDI-NIs. (**A**) Four equivalents of suitable diamine (1,2-diaminoethane for **NI-2**, 1,3-diaminopropane for **NI-3**, 1,4-diaminobutane for **NI-4**, and 1,7-diaminoheptane for **NI-7**), CH_3CH_2OH, reflux, 2 h; (**B**) CH_3CN, reflux, 16 h; (**C**) neat 2-(2-aminoethoxy)ethanol, 120°C, 250 psi, 10 min, microwave-assisted.

was almost completely quenched, suggesting a more pronounced aggregation under these conditions compared to MeOH (Supplementary Fig. S4). In summary, the fluorescence behavior correlates with the aggregation state: bright fluorescence is observed when the compounds are disaggregated, while aggregation leads to fluorescence quenching.

Study of hetero-dyads interaction with tel46, tel26, and ds12 model oligonucleotides by UV-vis and fluorescence spectroscopy

The investigated hetero-dyads were studied by UV-vis and fluorescence spectroscopy in their interaction with the following DNA models: (i) the 46-mer telomeric dimeric G4 of sequence d[AGGG (TTAGGG)$_7$] (tel46) [43, 44], (ii) the 26-mer telomeric monomeric G4 of sequence d (TTAGGGTTAGGGTTAGGGTTAGGGTT) (tel26) [43, 44], and (iii) the Dickerson B-DNA duplex of sequence d (CGCGAATTCGCG) (ds12) [45].

First, 5 μM NDI-NIs or DEG-NDI-NIs were added to solutions containing 5 μM oligonucleotides in 5 mM KH_2PO_4 buffer (pH 7.0) containing 150 mM KCl. This K^+ concentration was selected to mimic the physiological levels of this cation typically present in cells [46], strongly stabilizing G4 structures to better analyze their interaction with ligands. All solutions were left to equilibrate at r.t. for 4 h. Then UV-vis spectra were recorded to identify the CT band maxima, which have been used as excitation wavelengths for fluorescence experiments (Supplementary Fig. S5). Under these conditions, **NDI-NI-2**, **NDI-NI-3**, and **NDI-NI-4** exhibited complete fluorescence quenching in the presence of tel46 and tel26, with a moderate decrease when interacting with ds12 (Supplementary Fig. S5), suggesting an interaction between the NDI and NI components. This folding is likely driven by π–π stacking interactions and hydrophobic effects, which reduce the spatial separation between the chromophores. In the presence of tel46 and tel26 G4s, this folding is maximized, likely due to stronger binding or stabilization of the folded conformation upon G4 binding. In contrast, in the presence of ds12, the same ligands showed only a moderate quenching effect, possibly reflecting weaker or less specific interactions unable to fully stabilize the folded state. The fluorescence intensity of **NDI-NI-7**, on the other hand, was completely quenched only in the presence of tel26, suggesting different structural flexibility and intramolecular stacking toward monomeric and dimeric G4s. In contrast, DEG-NDI-NIs, which exhibit quenched fluorescence when dissolved alone in aq. solution, were activated in the presence of tel46 and tel26 G4s, suggesting a complete disaggregation of both inter- and intramolecular interactions (Supplementary Fig. S5). Unlike the NDI-NIs, this behavior highlights their inability to fold onto themselves in a sandwich-like conformation. Such a response aligns with the behavior previously reported for NDI-NDI dyads [22, 47], where interaction with G-quadruplex structures induced a "lighting up" effect attributed to the disruption of aggregated states and the formation of well-defined complexes with G4s (Fig. 1 right).

To further investigate ligands/oligonucleotide interactions, fluorescence titrations were performed in a 96-well microplate, by adding increasing amounts of each oligonucleotide (from 0 to 15 equiv.) to 5 μM solutions of NDI-NIs in 5 mM KH_2PO_4 buffer (pH 7.0) containing 150 mM KCl. After 4 h equilibration at r.t., fluorescence spectra were recorded. The results corroborated the preliminary findings: the fluorescence quenching of DEG-NDI-NIs in buffered aq. solution increased proportionally with the addition of tel46 and tel26 (Supplementary Figs S6–S8). This observation reinforces the hypothesis that these hetero-dyads interact with G-quadruplexes with one unit inserted into G4 stacking interfaces, while the other interacts with grooves or loops of adjacent G4s. In contrast, NDI-NIs exhibited enhanced fluorescence intensity in buffered aq. solution alone, but underwent complete fluorescence quenching upon addition of G4s (except for **NDI-NI-7** in the presence of tel46), consistent with self-folding behavior (Supplementary Figs. S9–S12). Nevertheless, despite the quenched signal, a slight fluorescence enhancement was observed for **NDI-NI-2**, **NDI-NI-3**, and **NDI-NI-4** only in the presence of tel46 G4. To better understand this behavior, the experiment was repeated using a 1 cm pathlength cuvette, optimizing parameters to enhance the fluorescence response. While **NDI-NI-2**, **NDI-NI-3**, and **NDI-NI-4** emission spectra increased in intensity upon binding tel46

G4, quenching of their fluorescence intensity was observed by adding tel26 G4 or ds12 duplex (Fig. 4 and Supplementary Figs S13–S15). **NDI-NI-7**, on the other hand, showed completely different features (Supplementary Fig. S16). Indeed, on increasing the oligonucleotide concentration, its emission first decreased, accompanied by a blue shift of the maximum, and then increased in the presence of both tel46 and tel26 G4s.

Interestingly, DEG-NDI-NIs exhibited lower overall binding affinities compared to NDI-NIs (Table 1), with a pronounced preference for monomeric tel26 (K_{11} values ranging from 8.3×10^5 to $12.8 \times 10^5\,M^{-1}$) over dimeric tel46 (K_{11} values ranging from 1.60×10^5 to $1.98 \times 10^5\,M^{-1}$) G4s. Binding to ds12 was significantly weaker, with high tel46/ds12 selectivity ratios (5.52–10.0).

In contrast, **NDI-NI-2**, **NDI-NI-3**, and **NDI-NI-4** showed higher binding affinities overall (Table 1), with comparable interactions for tel46 and tel26 (K_{11} values ranging from 9.0×10^5 to $13.8 \times 10^5\,M^{-1}$) and moderate selectivity over ds12 (K_{11} values from 2.9×10^5 to $4.0 \times 10^5\,M^{-1}$, with tel46/ds12 ratios of 3.07–4.07). **NDI-NI-7** exhibited a different behavior, with ∼30 times higher affinity for ds12 than the other NDI-NIs, and low selectivity for G4s, indicating distinct behavior driven by its structural features (Table 1). This comparison highlights the influence of the different ligand structures on binding specificity, with DEG-NDI-NIs favoring tel26 and discriminating ds12, while **NDI-NI-2**, **NDI-NI-3**, and **NDI-NI-4** exhibited tighter G4 binding and moderate duplex selectivity. The different behavior of **NDI-NI-7** could be attributed to its longer alkyl spacer, increasing the mobility of its NDI and NI units and thus enabling binding interactions with target DNA structures that differ significantly from those observed for the other NDI-NIs.

Circular dichroism studies

NDI-NIs and DEG-NDI-NIs were also studied by circular dichroism in their interaction with the same G4 and duplex models used in the fluorescence studies. The G4- and duplex-forming oligonucleotides were prepared by annealing the DNA solutions at 2 μM concentration in 20 mM KCl, 5 mM KH_2PO_4 buffer (pH 7). Under these conditions, the overall conformation, as derived by the CD profiles, and thermal stability of the analyzed oligonucleotides were as follows:

- tel46 folded into two hybrid-type G4s, featured by a positive band with a maximum at 291 nm, a shoulder at ca. 270 nm, and a weak positive band at 250 nm, and a melting temperature (T_m) value of 45°C (Supplementary Fig. S17A and B) [19];
- tel26 folded into a hybrid 2-type G4, featured by a positive band with a maximum centered at 289 nm and a shoulder at 267 nm, and a T_m value of 46°C (Supplementary Fig. S17C and D) [19];
- ds12 showed a positive band at 281 nm along with a negative one with a minimum at 253 nm, characteristic of a B-DNA duplex structure, and a T_m value of 66°C (Supplementary Fig. S17E and F) [45].

These secondary structure-forming oligonucleotides were titrated with increasing amounts of the hetero-dyads and the corresponding CD spectra recorded after each addition (Supplementary Figs S18–S24, left panels). CD-melting experiments were then performed on the 1:6 DNA/ligand systems to evaluate if stabilizing or destabilizing effects on the G4 and duplex models were obtained upon incubation with each ligand (Supplementary Figs S18–S24, right panels). All ligands produced significant conformational changes on the telomeric G4s. In contrast, lower (for **NDI-NI-2**, **NDI-NI-7**, **DEG-NDI-NI-3**, and **DEG-NDI-NI-4**) or even no effects (for **NDI-NI-3** and **NDI-NI-4**) were observed on the duplex model. Notably, only in the case of **DEG-NDI-NI-2** the effects on the duplex structure were more pronounced (Supplementary Figs S18–S24).

To get a deeper insight into the quantitative estimation of the composition of the mixtures of G4 structures formed by tel46 and tel26 in the absence and presence of the hetero-dyads in terms of parallel, hybrid and antiparallel G4 topologies, singular value decompositionanalysis was performed on the CD spectra by exploiting the software developed by del Villar-Guerra *et al.* [48]. Deconvolution analysis (Supplementary Table S2) showed that addition of 6 equiv. of each ligand resulted in a higher amount of hybrid folding for both tel46 and tel26 compared to the corresponding unbound G4s.

A summary of the stabilizing effects of all ligands on the target and the controls is reported in Table 2. A selectivity index was derived from the ratio between ΔT_m values for the tel46 G4 target and ΔT_m values for the control duplex. Good G4 versus duplex selectivity was found for all the hetero-dyads (ΔT_m ratios ≥ 1.7) with the exception of **DEG-NDI-NI-2**. Overall, NDI-NIs emerged as higher stabilizing ligands of telomeric G4s compared to DEG-NDI-NIs. In detail, **NDI-NI-3** emerged as the most stabilizing ligand of dimeric G4 structures, while **NDI-NI-4** was the one with the highest selectivity for the tel46 dimeric G4 over the duplex (Table 2).

Finally, **NDI-NI-2**, **NDI-NI-3**, and **NDI-NI-4** proved to have also an interesting ability to induce the G4 folding of tel46 sequence when initially unstructured. The behavior of **NDI-NI-3** was here reported as a representative case; for these experiments, a solution of tel46 dissolved in 10 mM Tris–HCl buffer (pH 7) i.e. in a metal cation-free system, in which the G-rich oligonucleotide is not folded in a G4 structure—was treated with 6 molar equiv. of **NDI-NI-3** and the CD spectra recorded (Supplementary Fig. S25A). Remarkably, unfolded tel46, when treated with **NDI-NI-3**, formed a hybrid G4 structure (Supplementary Fig. S25A, red line), featured by a T_m value of 33°C (Supplementary Fig. S25B).

In cell evaluation of NDI-NIs G4-stabilizing activity

As a preliminary experimental screening of the efficacy of the synthesized hetero-dyads, their ability to target and stabilize G4 structures was validated at the biological level by using two cellular models originating from tumors of different histotypes and showing differences in their mechanism of telomere maintenance [49, 50]. In detail, a telomerase-positive cervical carcinoma cell line, HeLa, and an alternative lengthening of telomeres (ALT)-positive osteosarcoma model, U2OS, were treated with the here studied ligands (0.5 μM for 24 h) and the number of G4 structures was evaluated by immunofluorescence (IF) confocal analysis by using an antibody, BG4, specific for these noncanonical secondary structures of nucleic acids [51]. As reported in Fig. 5, the two classes of ligands—NDI-NIs and DEG-NDI-NIs—showed very different biological effects. Indeed, while the NDI-NIs evidenced a marked capability of stabilizing G4 structures in both the cell lines, whereas the DEG-NDI-NIs, except for **DEG-NDI-NI-2**, did not

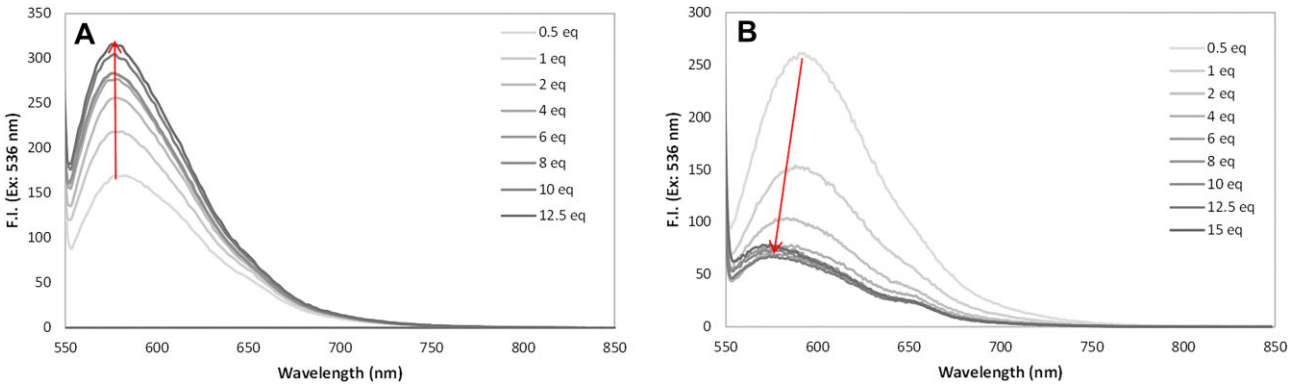

Figure 4. Fluorescence emission spectra of **NDI-NI-2** in the presence of the G4 targets. Emission spectra of 5 μM **NDI-NI-2** recorded after addition of increasing amounts of (**A**) tel46 and (**B**) tel26 in 150 mM KCl, 5 mM KH_2PO_4 buffer (pH 7.0), in 1 cm path length cuvette (slits of 10 nm, excitation filter auto, emission filter open, PMT = 800 V). Arrows indicate the variation of fluorescence intensity on increasing DNA concentration.

Table 1. Summary of K_{11} values

	K_{11} (x 10^5 M^{-1})			Ratio K_{11}	
	tel46	tel26	ds12	tel46/tel26	tel46/ds12
NDI-NI-2	11.8 ± 0.1	13.8 ± 0.2	2.9 ± 0.1	0.85	4.07
NDI-NI-3	9.9 ± 0.5	9.6 ± 0.4	3.0 ± 0.2	1.03	3.30
NDI-NI-4	12.3 ± 0.2	9.0 ± 0.2	4 ± 1	1.37	3.07
NDI-NI-7	3.1 ± 0.4	2.6 ± 0.6	126 ± 2	1.19	0.02
DEG-NDI-NI-2	1.98 ± 0.02	12.8 ± 0.4	0.198 ± 0.003	0.15	10.0
DEG-NDI-NI-3	1.75 ± 0.05	8.3 ± 0.9	0.176 ± 0.002	0.21	9.94
DEG-NDI-NI-4	1.60 ± 0.05	9.0 ± 0.2	0.29 ± 0.02	0.18	5.52

Binding constants for 1:1 stoichiometry for tel46 G4, tel26 G4, and ds12 duplex in the presence of the indicated hetero-dyads as obtained by fluorescence titration experiments (in a 1 cm path lenght cuvette for NDI-NIs and in a microplate reader for DEG-NDI-NIs). Data were processed by BindFit v0.5 online software [25].

Table 2. ΔT_m and ΔT_m ratio values for tel46 G4, tel26 G4, and ds12 duplex in the presence of **NDI-NI-2**, **NDI-NI-3**, **NDI-NI-4**, **NDI-NI-7**, **DEG-NDI-NI-2**, **DEG-NDI-NI-3**, and **DEG-NDI-NI-4** (six molar equivalents) as measured by CD melting experiments

	ΔT_m ± 1 (°C)			ΔT_m ratio	
Ligand/DNA	tel46	tel26	ds12	tel46/tel26	tel46/ds12
NDI-NI-2	+21	+16	+12	1.3	1.8
NDI-NI-3	+22	+20	+13	1.1	1.7
NDI-NI-4	+18	+22	+9	0.8	2.0
NDI-NI-7	+21	+23	+13	0.9	1.8
DEG-NDI-NI-2	+14	+14	+16	1.0	0.88
DEG-NDI-NI-3	+10	+9	+6	1.1	1.7
DEG-NDI-NI-4	+10	+6	+6	1.7	1.7

$\Delta T_m = T_m$ (DNA/ligand, 1:6) − T_m (free DNA).

recapitulate their activity in the evaluated cell models, indicating that the introduction of the 2-(2-aminoethoxy)ethanol side-chain negatively affects the cellular behavior of the NDI-NIs.

Biological evaluation of hetero-dyads

Considering the high biological relevance of G4 stabilizing agents in cancer biology, all the synthesized NDI-NIs were then evaluated for their ability to affect cell viability. To this aim, BJ-EHLT, an engineered cell line obtained from BJ fibroblast through a dual process of immortalization and transformation [26], underwent treatment with multiple concentrations (ranging from 0.1 to 1 μM) of the different hetero-dyads and, after 48 h, they were processed for crystal violet assays. Notably, as reported in the figure (Fig. 6A, left panel), **NDI-NI-2**, **NDI-NI-3**, and **NDI-NI-4** promoted a robust and significative impairment of cell viability, with an IC_{50} value corresponding to the concentration of drug effective in inhibiting by half a biological process of ∼0.5 μM. Conversely, **NDI-NI-7** and **DEG-NDI-NI-2**, even promoting G4 stabilization (Fig. 5), showed very poor or no activity in these experiments. This suggests that these two compounds at the evaluated time and doses promote slight and/or transient damages that are then rescued by cellular mechanisms of DDR. Finally, as expected, the two compounds that were unable to stabilize G4s (**DEG-NDI-NI-3** and **DEG-NDI-NI-4**) did not promote DNA damage in the evaluated cell models. Concomitantly, the NDI-NIs were also tested on BJ-hTERT, a cell line obtained from the sole immortalization of the BJ fibroblasts, which can be reasonably considered the "normal" counterpart of BJ-EHLT. Interestingly, the results of viability assays demonstrated that these cells were almost insensitive to treatment with all the tested compounds (Fig. 6A), indicating that these ligands are selectively effective against transformed cells.

Then, based on literature data showing that antitumoral activity of G4 ligands is mainly attributable to the capability of these molecules of inducing DNA damage, BJ-EHLT cells were treated with the different NDI-NIs and DEG-NDI-NIs and the levels of phosphorylated histone H2AX (γH2AX), a hallmark of double-strand breaks [52], were evaluated. Interestingly, immunofluorescence (IF) experiments demonstrated that **NDI-NI-2**, **NDI-NI-3**, and **NDI-NI-4** showed effectiveness in viability assays and promoted a robust and significative

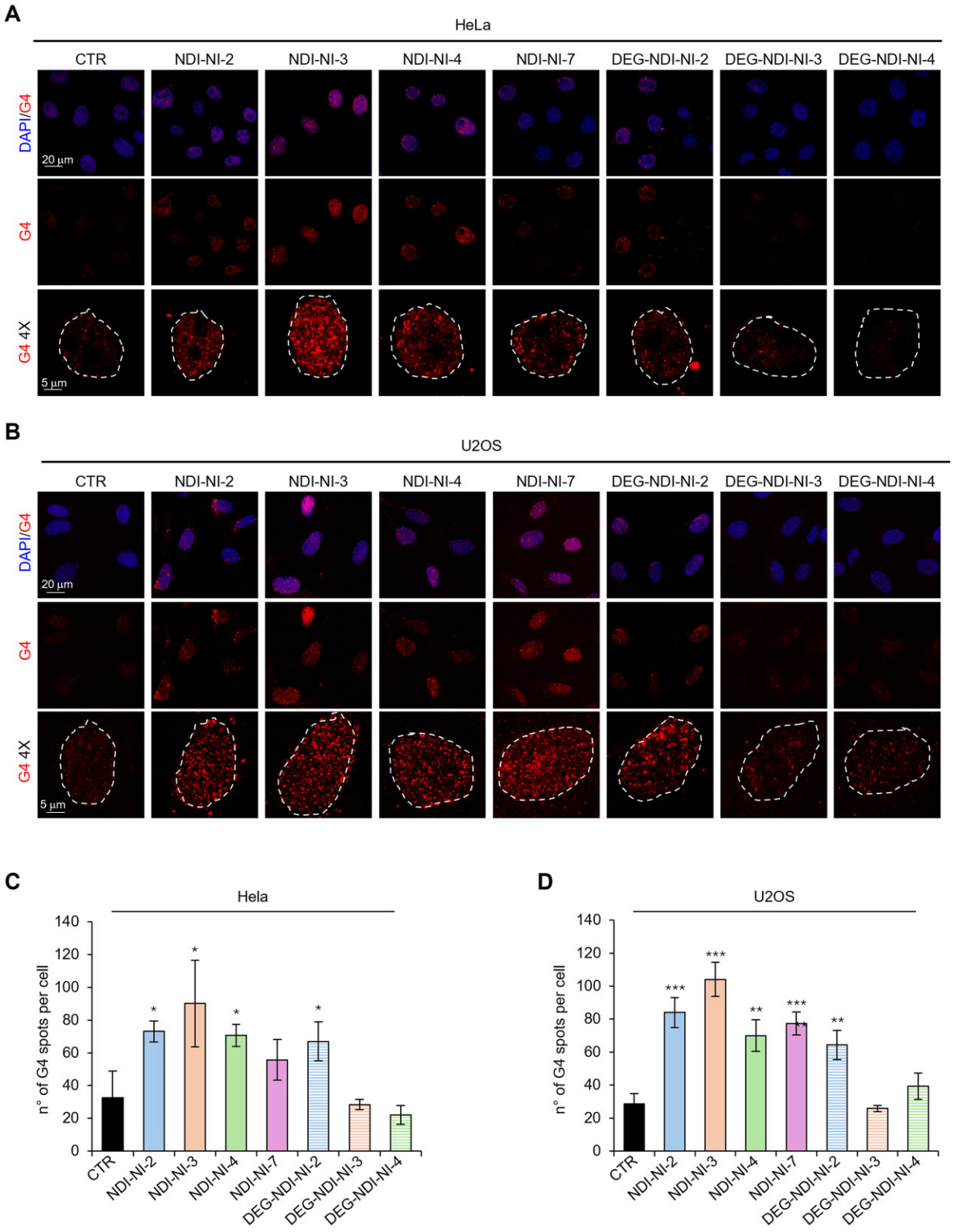

Figure 5. NDI-NIs stabilized G-quadruplex structures in cells. Immunofluorescence evaluation of G4 structures in human cervical HeLa and osteosarcoma U2OS cancer cell lines. The cells were treated with the indicated compounds at a final concentration of 0.5 μM for 24 h and then processed for immunofluorescence with an antibody specific for G4 structures (anti-BG4). (**A**, **B**) Representative images acquired by confocal microscopy (magnification 63X) of HeLa (A) and U2OS (B). G4 structures are labeled in red, while cell nuclei are stained with DAPI (blue). 4× enlargements of selected regions (white squares) are shown. Scale bars indicate 5 μm. (**C**, **D**) Quantification of the number of G4 structures in HeLa (C) and U2OS (D) cells. At least 30 cells for each condition were counted. The histograms represent the mean values ± S.D. of three independent experiments. $*P < .05$, $**P < .01$, and $***P < .001$.

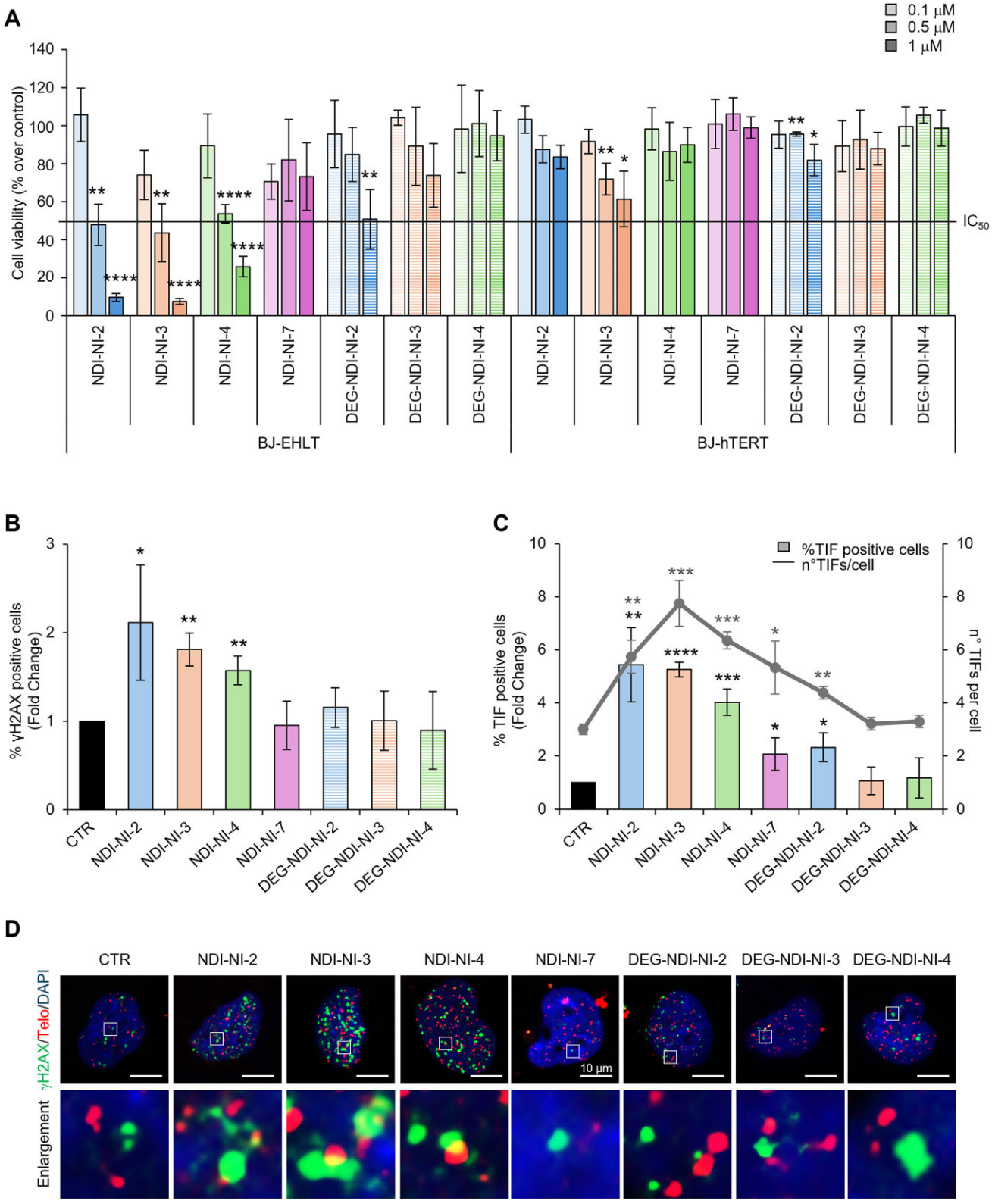

Figure 6. Biological activity evaluation of NDI-NIs and DEG-NDI-NIs. (**A**) Cell viability assays performed in human foreskin-derived fibroblast (BJ), expressing the human telomerase reverse transcriptase hTERT and SV40 early region (BJ-EHLT) or only hTERT (BJ-hTERT) and treated with the indicated compounds for 48 h at the final concentrations of 0.1, 0.5, and 1 μM. The results were expressed as the percentage of cell viability over the untreated cells. (B–D) BJ-EHLT cells were treated with the indicated compound for 24 h at a final concentration of 0.5 μM and, successively, processed for telomeric FISH combined with immunofluorescence experiments using the antibody against γH2AX, a marker of the DNA damage. (**B**) Percentage of γH2AX positive cells. (**C**) Quantitative analysis of the number of telomere induced foci (TIF) per cell and of the percentage of TIF positive cells. Cells with at least four γ-H2AX/Telo colocalizations were scored as TIF positive. (**D**) Representative images of the experiment in panels (B) and (C), acquired by confocal microscopy (magnification 63×). Scale bars indicate 10 μm. The histograms represent the mean values ± S.D. of three independent experiments. *$P < .05$, **$P < .01$, ***$P < .001$, and ****$P < .0001$.

enhancement of DNA damage (Fig. 6B). Subsequently, based on the biophysical experiments which evidenced affinity of NDI-NIs for telomeric G4s, the capability of these molecules to effectively target the terminal portion of chromosomes in cells was evaluated. To this aim, IF analyses of DNA damage were combined with FISH assays, and the TIF—fluorescent spots deriving from the colocalization of γH2AX and the telomeric probe signals—were quantified. Notably, the results of confocal analyses evidenced that at least 50% of the cells treated with **NDI-NI-2**, **NDI-NI-3**, or **NDI-NI-4** were TIF positive (TIF ≥ 4), indicating that the reduced cell viability observed in response to NDI-NIs might be reasonably correlated with the capability of these molecules of inducing a telomere-localized DNA damage (Fig. 6C and D).

Finally, to define the potency of this new class of G4 ligands, the activity of the new hetero-dyads was compared with that of two widely studied G4 ligands: the pentacyclic acridine 3,11-difluoro-6,8,13-trimethyl-8H-quino[4,3,2-kl]acridinium methosulfate (RHPS4), which is known to exert telomere-directed activity and the N,N′-bis (quinolinyl)pyridine-2,6-dicarboxamide (Pyridostatin, PDS), a G4 ligand with a non-telomere-directed activity [53]. Due to the different chemical nature of the evaluated compounds, RHPS4 and PDS were first assayed for their capability to stabilize G4s at the same dose and time of the NDI-NIs (0.5 μM for 24 h). Notably, IF experiments performed with the anti-BG4 antibody demonstrated that RHPS4 and PDS promoted G4 stabilization to the same extent as the NDI-NIs (Figs 5C, D, and 7A, B), thus indicating that these different G4 ligands can be compared under the same experimental conditions. Then, RHPS4 and PDS were tested also for their antiproliferative and DNA-damaging activities. Interestingly, viability assay evidenced that the two ligands, almost ineffective on normal cells (BJ-hTERT), promoted a dose- and time-dependent antiproliferative activity in BJ-EHLT fibroblasts (Fig. 7C and D), showing an IC_{50} value of ∼1 μM at 96 h. Moreover, analyses of DNA damage evidenced that the two known ligands, as expected, produced a robust accumulation of DNA damage that, in the case of RHPS4, was largely localized also at telomeres (Fig. 7E–G). Interestingly, the comparison of these results with those obtained with the NDI-NIs (Fig. 6) highlights that this new class of compounds—while working at lower doses and at shorter times than RHPS4 and PDS—promotes tumor-selective antiproliferative activity to the same extent as the two reference compounds, showing telomere specificity similar to RHPS4.

Evaluation of NDI-NIs as antitumoral agents

BJ-EHLT and BJ-hTERT, deriving from the same cell line of origin, represent a valid tool to demonstrate the capability of a drug to discriminate between transformed cells and their normal counterpart. However, BJ-ELTH cells do not represent a real cancer cell model and, as such, they can not be used to establish the antitumoral efficacy of new potential drugs. Based on these considerations, the most promising NDI-NIs (**NDI-NI-2**, **NDI-NI-3**, and **NDI-NI-4**) were evaluated in a panel of human cell lines originating from tumors of different histotypes: cervix (HeLa), colon (HT29 and HCT116), bone (U2OS and MG63), and breast (MDA-MB-231 and MDA-MB-436) (Fig. 8 and S26A).

These results, summarizing the data previously obtained in BJ-EHLT (Fig. 6A), demonstrated that the selected ligands are able to impair the viability of all the evaluated cell lines, independently from the histotype and the mechanism of telomere maintenance. Indeed, the tested ligands produced similar effects in both telomerase-positive (Fig. 8A and C) and telomerase-negative cells (Fig. 8B). The same analyses—despite intrinsic limitations deriving from the low number of evaluated cell lines—suggest that the activity of screened compounds is not dependent on the genetic background of the target cells. Indeed, the three G4 ligands (**NDI-NI-2**, **NDI-NI-3**, and **NDI-NI-4**) promoted similar effects in U2OS and MG63, two ALT cell lines differing in the mutational status of the tumor suppressor gene TP53 (Fig. 8B). Similarly, the ligands proved to be effective in both BRCA-proficient (MDA-MB-231) and -deficient (MDA-MB-436) cells (Fig. 8C), indicating that these compounds—differently from other known G4 stabilizing agents [27]—exert their activity also in cells able to repair the DNA damage. To corroborate these data, the activity of the NDI-NIs was also evaluated in HCT116 cells genetically depleted for TP53 (HCT116 $TP53^{-/-}$) or BRCA2 (HCT116 $BRCA2^{-/-}$). Interestingly, the results of viability assays evidenced no differences in the drug responses of both the engineered cells and their wild-type counterpart (HCT116 WT), confirming the previous results also in cell models sharing the same genetic background (Supplementary Fig. S26A).

Finally, to improve the translational relevance of our data, the NDI-NIs were tested in spheroids obtained from HCT116, an easy-to-handle cell line already tested for sensitivity to these molecules (Supplementary Fig. S26). Notably, these advanced 3D models recapitulate, *in vitro*, the spatial architecture and the complexity of a tumor mass and, as such, represent a valid alternative to using animal models [54]. In particular, time-course analyses, performed both in absence and presence of the tested ligands, demonstrated the efficacy of NDI-NIs in impairing the spheroids growth (Fig. 9A and B). In line with these data, immunohistochemical analyses performed on spheres treated with the highest tested dose of each compound (5 μM), highlighted the capability of the NDI-NIs to reduce proliferation, as defined by Ki67 (Fig. 9C). Furthermore, **NDI-NI-3**, the most effective ligand in impairing sphere growth, was found to induce cell death associated with a robust and significative enhancement of DNA damage, evaluated by cleaved Caspase-3 and γH2AX signal, respectively (Fig. 9C). The collected data, demonstrating the effectiveness of NDI-NIs in promoting a potent antitumoral activity, also in advanced *in vitro* models, paved the way to further investigations aimed at consolidating the clinical application of this new class of G4 ligands.

Molecular docking analysis

To assess the ability of the newly designed hetero-dyads to target multimeric G4s at their internal binding pocket, molecular docking studies were performed for all the compounds with a model of telomeric dimeric G4, i.e. tel45, containing a G4-G4 interface. Additionally, a telomeric monomeric G4 model (tel26) and a B-DNA duplex model (ds12) were used as controls.

In the case of the interaction of the best performing **NDI-NI-2**, **NDI-NI-3**, and **NDI-NI-4** compounds with tel45 G4, the most populated cluster involved completely folded hetero-dyads within the binding pocket at the G4-G4 interface (Supplementary Fig. S27), thus supporting the ability of these compounds designed as G4-G4 interface binders to specifically recognize the desired binding site of the G4 target. In-

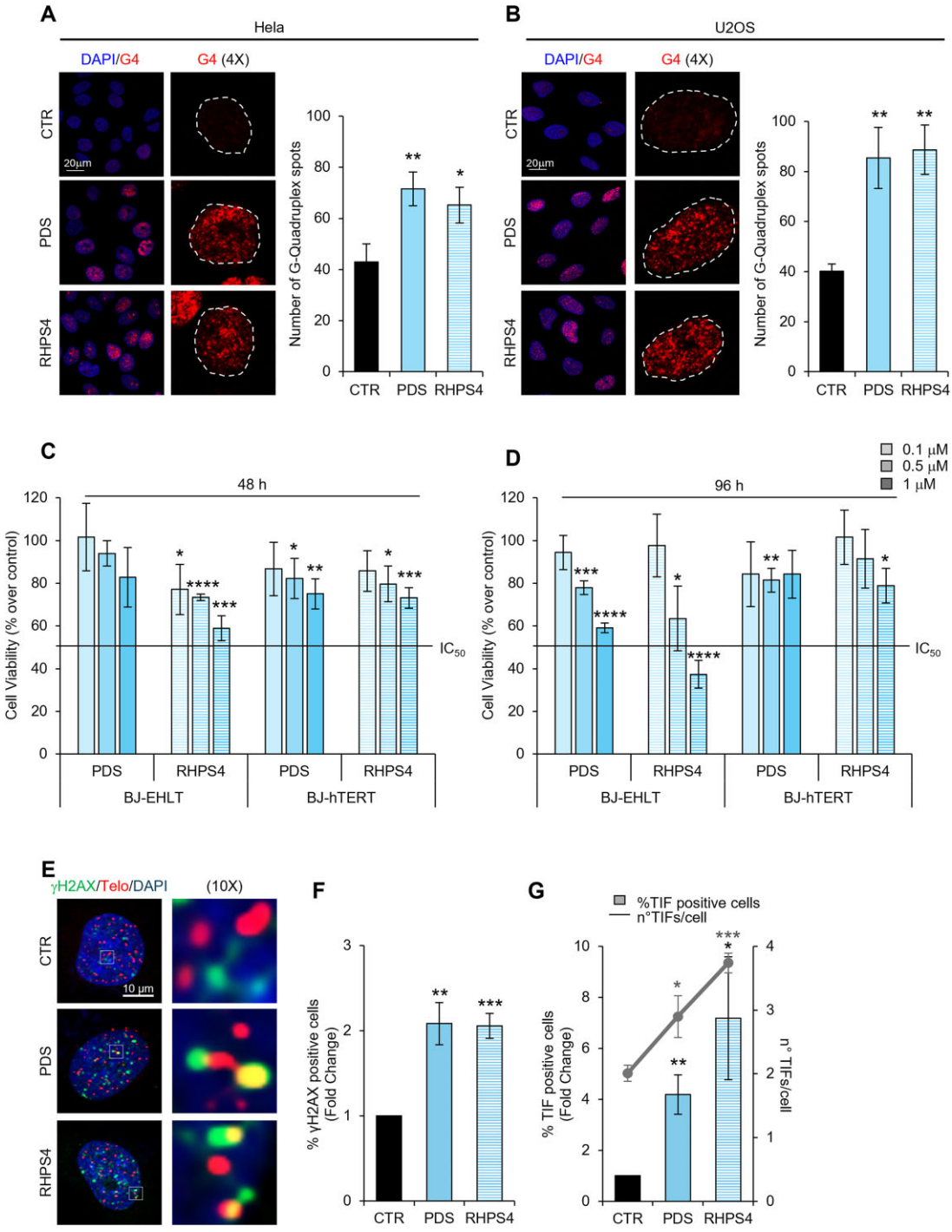

Figure 7. Biological activity evaluation of RHPS4 and Pyridostain. (**A**, **B**) Immunofluorescence evaluation of G4 structures in human cervical HeLa (A) and osteosarcoma U2OS (B) cancer cell lines. The cells were treated with the telomere-directed pentacyclic acridine 3,11-difluoro-6,8,13-trimethyl-8H-quino[4,3,2-kl]acridinium methosulfate (RHPS4) and the non-telomere-directed N,N′-bis (quinolinyl)pyridine-2,6-dicarboxamide (Pyridostatin, PDS) at the final concentration of 0.5 μM for 24 h and then processed for immunofluorescence with the specific antibody for G4 structures (anti-BG4). *Left panels*: representative images acquired by confocal microscopy (magnification 63×). G4 structures are labeled in red and the nuclei are stained with DAPI (blue). 4× enlargements of selected regions (white squares) are shown. Scale bars indicate 20 μm. *Right panels:* Quantification of the number of G4 structures per cell. At least 30 cells for condition were counted. The histograms represent the mean values ± S.D. of three independent experiments. $*P < .05$, $**P < .01$, and $***P < .001$. (**C**, **D**) Cell viability assays performed in human foreskin-derived fibroblast (BJ), expressing the human telomerase reverse transcriptase hTERT and SV40 early region (BJ-EHLT) or only hTERT (BJ-hTERT) and treated with PDS and RHPS4 at the final concentrations of 0.1, 0.5, and 1 μM for 48 (C) and 96 (D) h. The results were expressed as the percentage of cell viability over the untreated cells. (E–G) BJ-EHLT cells were treated with the indicated compound for 24 h at a final concentration of 0.5 μM and, successively, processed for telomeric FISH combined with immunofluorescence experiments using the antibody against γH2AX, a marker of the DNA damage. (**E**) Representative images acquired by confocal microscopy (magnification 63×). Scale bars indicate 10 μm. (**F**) Percentage of γH2AX positive cells. (**G**) Quantitative analysis of the number of TIF per cell and of the percentage of TIF positive cells. Cells with at least four γ-H2AX/Telo colocalizations were scored as TIF positive. The histograms represent the mean values ± S.D. of three independent experiments. $*P < .05$, $**P < .01$, $***P < .001$, and $****P < .0001$.

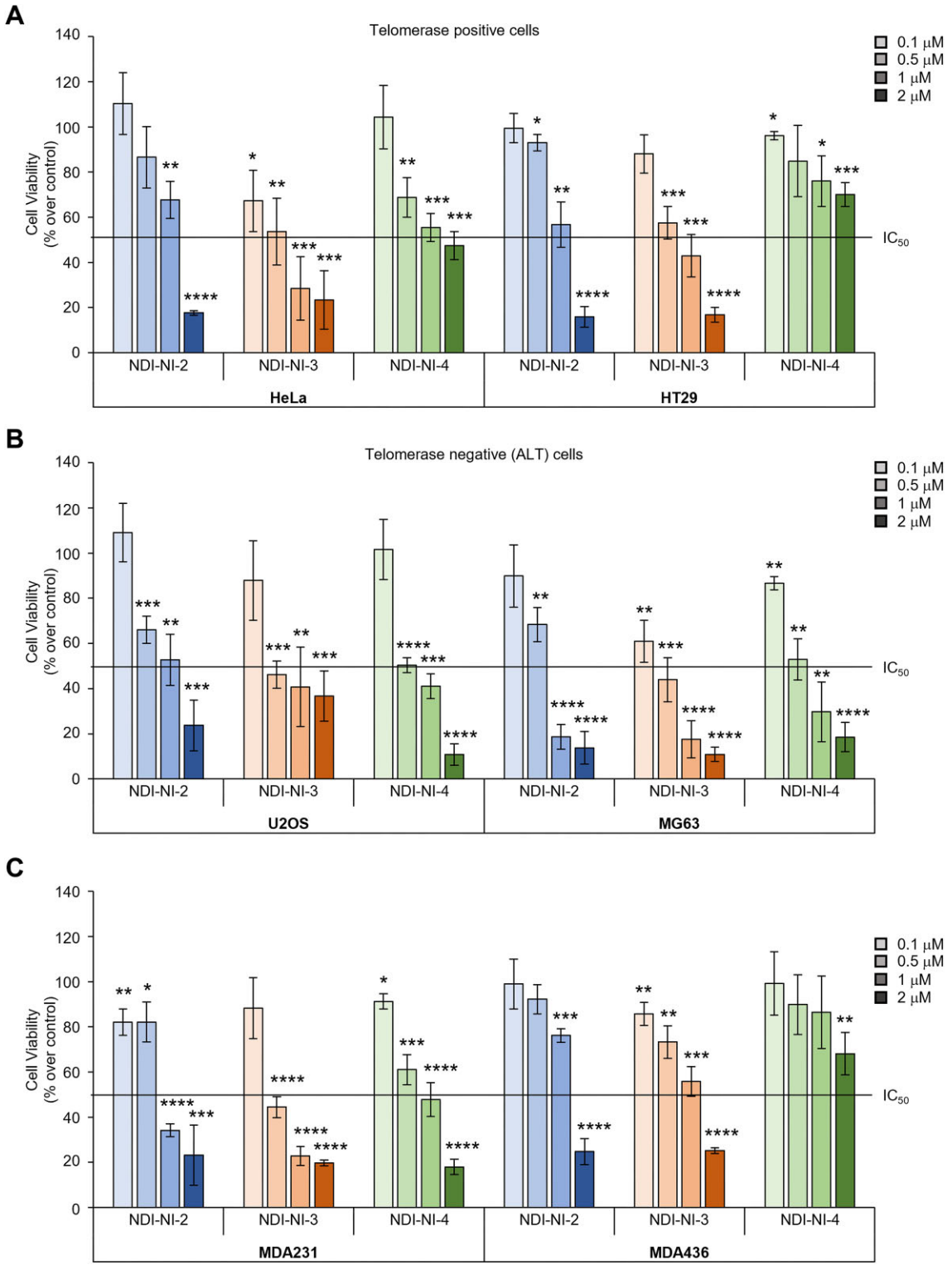

Figure 8. Antitumoral efficacy of NDI-NIs is independent from tumor histotype, telomerase activity, and BRCA status. Human cervical (HeLa), colorectal (HT29) (**A**), bone (U2OS and MG63) (**B**), and breast (MDA-MB-231 and MDA-MB-436) (**C**) cancer cells were treated with the indicated compounds for 48 h and processed for cell viability assay. The histograms represent the mean values ± S.D. of three independent experiments, expressed as a percentage of cell viability over the untreated cells. $^{*}P < .05$, $^{**}P < .01$, $^{***}P < .001$, and $^{****}P < .0001$.

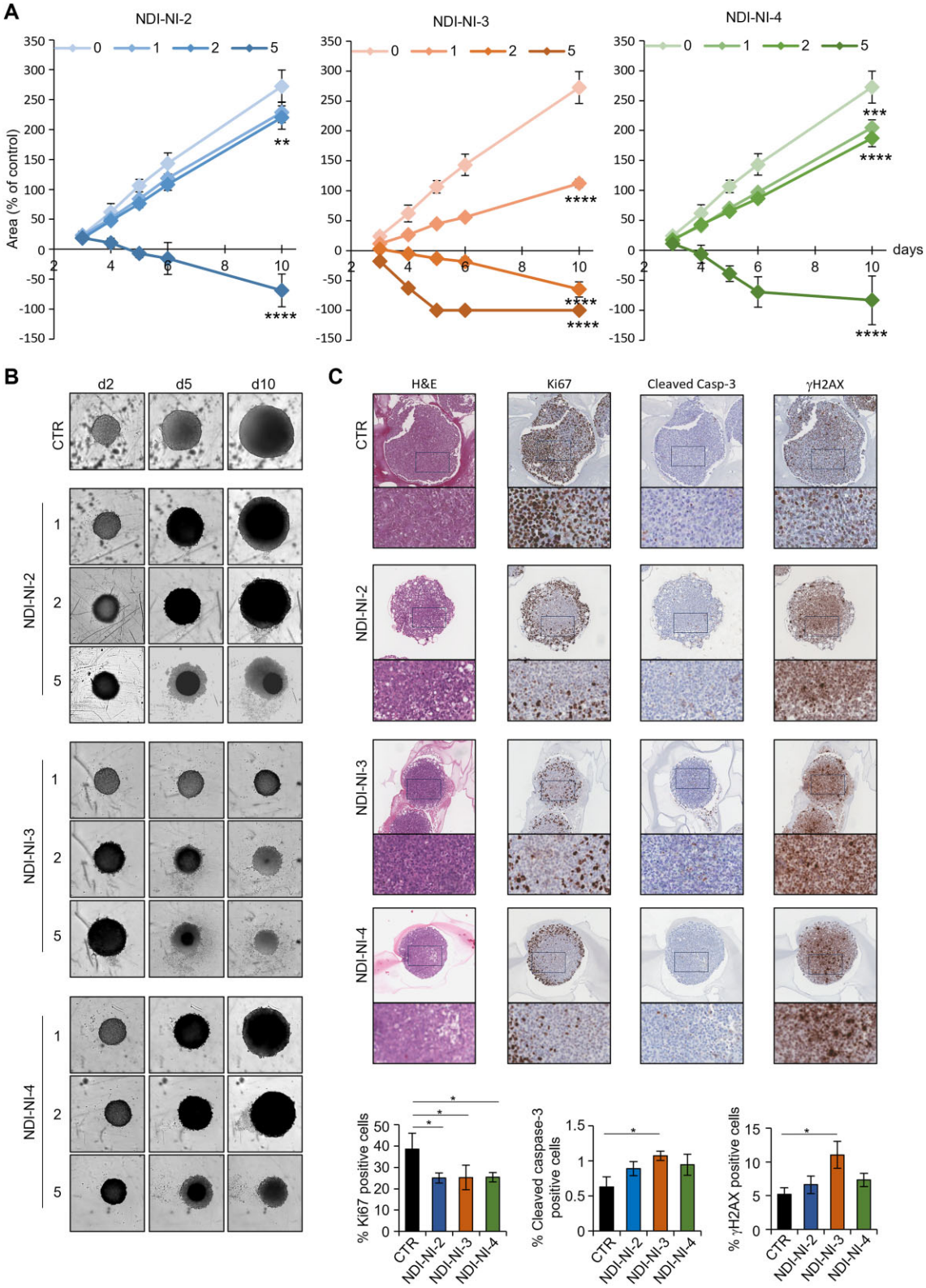

Figure 9. Antitumoral efficacy of NDI-NIs in advanced 3D models. Advanced 3D spheroids were established from human colorectal cancer cells (HCT116) by growing the cells within drops of a methylcellulose scaffold matrix (day 0). After 2 days of culture (day 2), the spheres were treated with the indicated compound at final concentrations of 1, 2, and 5 μM. (**A**) Time course analysis of tumor spheroids growth, starting from 24 h after treatment (day 3), monitored by Incucyte® S3 Live-Cell Analysis System (Essen BioScience, Ann Arbor, MI), 10× magnification. The results were expressed as the percentage of the spheroids area upon treatment relative to their own area before the compound administration. The histogram represents the mean values ± S.E.M. of at least four spheres. (**B**) Representative images of tumor spheroids growth described in panel (A). (**C**) Histological and immunohistochemical analysis of the spheroids generated from HCT116 cell lines and grown as in panel (A). *Upper panels,* representative images of immunostained sections. Lower panels, quantification of Ki-67, cleaved-caspase and γH2AX levels, expressed as percentage of positive cells. Thirty fields for condition were analyzed. The histograms represent the mean values ± S.D. of three independent experiments. $^{*}P < .05$, $^{**}P < .01$, $^{***}P < .001$, and $^{****}P < .0001$.

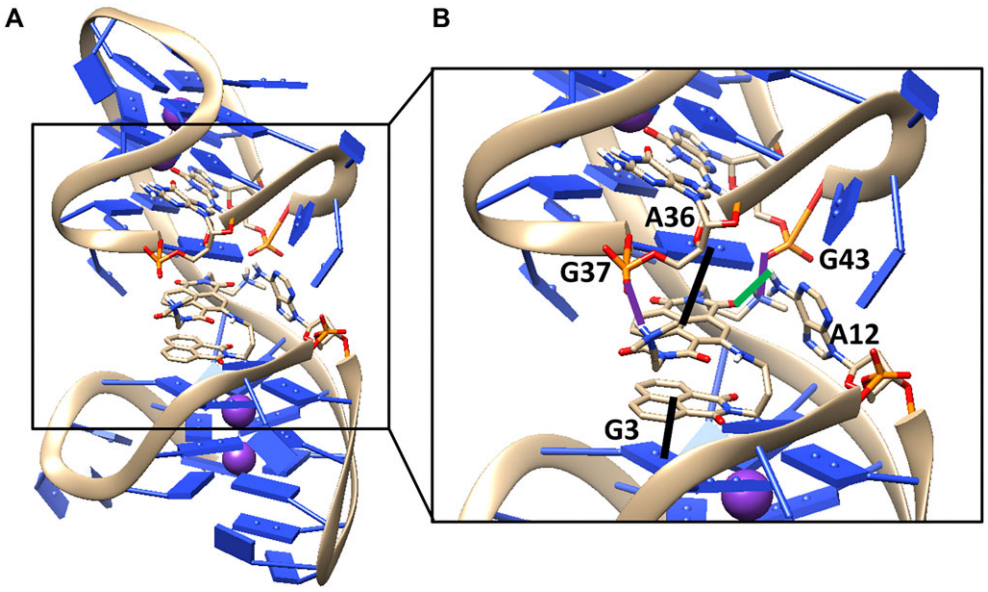

Figure 10. MD simulations on the tel45/N**DI-NI-3** complex. (**A**) Snapshot from the last frame of the 1 μs MD simulation performed for the tel45/**NDI-NI-3** complex. (**B**) Enlargement of the binding pocket formed by the G4 units of the tel45 dimeric G4, which highlights the interactions between the tel45 dimeric G4 and **NDI-NI-3**. The tel45 dimeric G4 and **NDI-NI-3** are shown as ribbon and sticks, respectively, while K^+ ions are represented as purple spheres. Stacking interactions, hydrogen bonds, and electrostatic interactions are shown as black, green, and purple bold lines, respectively. Nucleotides involved in the interactions are labeled.

terestingly, the NDI and NI units of **NDI-NI-3** and **NDI-NI-4** were stacked on top of each other within the G4-G4 binding pocket, whereas in the case of **NDI-NI-2**, the two units were unstacked. A different binding mode was observed for **NDI-NI-7**, which was found to be only partially inserted in the binding pocket with one unit close to the groove of one of the two adjacent G4s, in agreement with the peculiar behavior observed by the above biophysical techniques for this ligand compared to the other ligands here investigated. The binding energy for these poses was between −7.7 and −10.9 kcal/mol (Supplementary Table S3).

In the case of tel26 monomeric G4, all the hetero-dyads targeted the 5′-end residues of the G4, in all cases adopting a sandwich-like conformation wherein the two units, and particularly the NDI units, were stacked on the 5′-end residues (Supplementary Fig. S28). The binding energy for these poses was between −6.2 and −7.0 kcal/mol (Supplementary Table S3). On the other hand, the most populated cluster in the binding to the ds12 duplex showed interactions with its major groove and in detail with the central part of this groove, wherein each ligand was bound in a sandwich-like conformation (Supplementary Fig. S29), with binding energies comprised between −6.1 and −6.7 kcal/mol (Supplementary Table S3).

Remarkably, the trend of the binding energies obtained by docking analysis indicated a preference of the ligands for the tel45 dimeric G4 compared to the tel26 monomeric G4, as well as a very good G4 vs. duplex selectivity in agreement with the biophysical characterization findings reported above (Supplementary Table S3).

MDs simulations

Considering the significant results obtained in preclinical cancer models for **NDI-NI-3**, its interaction with the tel45 dimeric G4 was more in-depth investigated using MDs simulations. The docking complex tel45/**NDI-NI-3**, as well as the free tel45 dimeric G4, were subjected to 1 μs of unrestrained MD simulations (see "Experimental" section for details). The resulting MD trajectory showed that the free tel45 dimeric G4 has high flexibility and a dynamic structure (Supplementary Figs S30A and S31A), in full agreement with recent experimental data on multimeric telomeric G4 structures [8]. In detail, although the hybrid 1 and hybrid 2 conformations of each G4 unit were preserved, the two G4 units moved independently rotating around the TTA linker with rearrangements of the flanking end and loop residues (Supplementary Fig. S30A). Moreover, the two central axes of the two G4s formed an angle of ca. 90 degrees at the end of the MD simulation (Supplementary Fig. S31A).

Notably, the high structural flexibility of the free tel45 dimeric G4 was reduced in the presence of bound **NDI-NI-3** along the 1 μs simulation (Supplementary Figs S30 and S31). Interestingly, the hybrid-1 and hybrid-2 G4 units remained close enough during the whole simulation, thus forming a binding pocket wherein **NDI-NI-3** was stably inserted (Supplementary Fig. S32B and Fig. 10A). In detail, at the end of the simulation, the NDI and NI units of the ligand were stably stacked one on top of the other (Fig. 10A), and in turn, the NDI unit was stacked on A36 and the NI unit on G3 of the tel45 dimeric G4, respectively (highlighted with black lines in Fig. 10B). Additionally, the negatively charged phosphate groups of G37 and G43 interacted with the protonated amino groups on the two opposite side chains of **NDI-NI-3** (highlighted with purple lines in Fig. 10B; electrostatic interactions were observed in 94% and 66% of the simulation time, respectively), while a hydrogen bond formed between the hydrogen on N6 of A12 and one of the oxygen atoms of the NDI unit (highlighted with green line in Fig. 10B; hydrogen bond observed in 67% of the simulation time).

Overall, MD simulations, in agreement with docking analysis, clearly showed that **NDI-NI-3** was well accommodated

into the binding pocket at the interface of the two G4 units within the tel45 dimeric G4. Notably, the **NDI-NI-3** binding induced a compacting of the tel45 dimeric G4 and a reduction of its dynamic behavior compared to the free tel45 dimeric G4.

Conclusions

Based on the research findings proving the biological significance of multimeric G4 structures within telomeres, we here designed and synthesized a new class of ligands tailored to selectively target and stabilize them. These compounds are featured by NDI-NI hetero-dyads systems engineered to specifically interact with the unique binding pocket formed between two consecutive G4 structures in telomeres. Within the set of newly synthesized compounds, **NDI-NI-2**, **NDI-NI-3**, and **NDI-NI-4** emerged as the most potent and selective G4 ligands, exhibiting enhanced affinity and selectivity for the dimeric G4 model tel46. Computational analysis and biophysical assays suggested that their selectivity could be ascribed to their specific binding mode. Notably, **NDI-NI-2**, **NDI-NI-3**, and **NDI-NI-4** exhibited the peculiar ability to interact specifically within the binding pocket between two contiguous G4s, cooperatively interacting with both binding units. These properties correlated with the biological assays here carried out. Specifically, **NDI-NI-2**, **NDI-NI-3**, and **NDI-NI-4** showed marked antiproliferative effects against human cells of tumoral origin and no activity on healthy cells. The analysis of DNA damage revealed high γH2AX values, with localization predominantly at the telomeres. Moreover, our study validated the preclinical efficacy of NDI-NIs in different cancer cell models. Notably, the selected ligands evidenced a robust antitumoral activity in a panel of human cell-lines originating from different tumor histotypes, overcoming the limitations observed for other G4 ligands and related to DNA repair mechanisms. The ligands proved to be effective in both 2D and advanced 3D models, showcasing their potential translational relevance. Additionally, their impact on spheroid growth was corroborated by immunohistochemical analyses, evidencing alterations in proliferation and cell death markers. However, while our results support the biological relevance of NDI-NIs as G4 binders, the moderate selectivity for telomeric G4s in biophysical studies does not rule out the possible contribution of additional mechanisms. Taken together, these results highlight the huge potential of **NDI-NI-2**, **NDI-NI-3**, and **NDI-NI-4** as antitumoral agents and pave the way for further investigations to assess the clinical applicability of these molecules in cancer therapy.

Acknowledgements

C.P. was supported by Fondazione Umberto Veronesi. The research leading to these results has received funding from Fondazione AIRC under IG 2020—ID 25046—P.I. Montesarchio Daniela; IG 2018—ID 21579—P.I. Biroccio Annamaria; CN00000041 National Center for Gene Therapy and Drugs based on RNA Technology, and the European Union-NextGeneration EU—P.I. Montesarchio Daniela.

Author contributions: Valentina Pirota (Conceptualization, Data curation, Formal analysis, Investigation, Methodology, Validation, Writing—original draft, Writing—review & editing), Sara Iachettini (Data curation, Formal analysis, Investigation, Methodology, Validation, Writing—original draft, Writing—review & editing), Chiara Platella (Conceptualization, Data curation, Formal analysis, Investigation, Methodology, Validation, Writing—original draft, Writing—review & editing), Pasquale Zizza (Conceptualization, Data curation, Investigation, Methodology, Project administration, Supervision, Writing—original draft, Writing—review & editing), Giorgia Fracchioni (Data curation, Formal analysis), Serena Di Vito (Formal analysis), Alice Carachino (Formal analysis), Federica Battistini (Formal analysis), Modesto Orozco (Data curation, Validation), Mauro Freccero (Data curation, Funding acquisition), Annamaria Biroccio (Data curation, Funding acquisition, Project administration, Supervision, Writing—review & editing), Daniela Montesarchio (Conceptualization, Funding acquisition, Project administration, Supervision, Writing—review & editing), Filippo Doria (Conceptualization, Funding acquisition, Project administration, Supervision, Writing—original draft, Writing—review & editing)

Supplementary data

Supplementary data is available at NAR online.

Conflict of interest

None declared.

Funding

European Union; Fondazione Umberto Veronesi; EU; National Center for Gene Therapy and Drugs [21579, CN00000041, IG 2018]; Fondazione AIRC [25046, IG 2020].

Data availability

The data underlying this article are available in the article and in its online supplementary material. Additional material or information can be provided upon request by contacting the corresponding author.

References

1. Varshney D, Spiegel J, Zyner K *et al.* The regulation and functions of DNA and RNA G-quadruplexes. *Nat Rev Mol Cell Biol* 2020;**21**:459–74. https://doi.org/10.1038/s41580-020-0236-x
2. Asamitsu S, Shioda N, Sugiyama H. Telomeric quadruplexes as therapeutic targets. In: Neidle S (ed.), *Annual Reports in Medicinal Chemistry*. Academic Press, Vol. **54**, 2020, 77–99.
3. Salvati E, Rizzo A, Iachettini S *et al.* A basal level of DNA damage and telomere deprotection increases the sensitivity of cancer cells to G-quadruplex interactive compounds. *Nucleic Acids Res* 2015;**43**:1759–69. https://doi.org/10.1093/nar/gkv006
4. Doria F, Pirota V, Petenzi M *et al.* Oxadiazole/pyridine-based ligands: a structural tuning for enhancing G-quadruplex binding. *Molecules* 2018;**23**:2162. https://doi.org/10.3390/molecules23092162
5. Figueiredo J, Carreira-Barral I, Quesada R *et al.* Synthesis and evaluation of 2,9-disubstituted-1,10-phenanthroline derivatives as G-quadruplex binders. *Bioorg Med Chem* 2022;**73**:116971. https://doi.org/10.1016/j.bmc.2022.116971
6. Zhao C, Wu L, Ren J *et al.* Targeting human telomeric higher-order DNA: dimeric G-quadruplex units serve as preferred binding site. *J Am Chem Soc* 2013;**135**:18786–9. https://doi.org/10.1021/ja410723r

7. Kolesnikova S, Hubálek M, Bednárová L *et al.* Multimerization rules for G-quadruplexes. *Nucleic Acids Res* 2017;**45**:8684–96. https://doi.org/10.1093/nar/gkx637
8. Monsen RC, Chakravarthy S, Dean WL *et al.* The solution structures of higher-order human telomere G-quadruplex multimers. *Nucleic Acids Res* 2021;**49**:1749–68. https://doi.org/10.1093/nar/gkaa1285
9. Lu F, Zhang M-J, Li J-H *et al.* NIR imaging human telomeric dimeric G-quadruplexes by malachite green dimers and their antitumor activity. *Dyes Pigm* 2022;**203**:110307. https://doi.org/10.1016/j.dyepig.2022.110307
10. Zhao J, Yang Z, Zhai Q *et al.* Specific recognition of telomeric multimeric G-quadruplexes by a simple-structure quinoline derivative. *Anal Chim Acta* 2020;**1132**:93–100. https://doi.org/10.1016/j.aca.2020.07.017
11. Zhao J, Zhai Q. Recent advances in the development of ligands specifically targeting telomeric multimeric G-quadruplexes. *Bioorg Chem* 2020;**103**:104229. https://doi.org/10.1016/j.bioorg.2020.104229
12. Hu M-H, Chen S-B, Wang B *et al.* Specific targeting of telomeric multimeric G-quadruplexes by a new triaryl-substituted imidazole. *Nucleic Acids Res* 2017;**45**:1606–18. https://doi.org/10.1093/nar/gkw1195
13. Yu H, Gu X, Nakano S-i *et al.* Beads-on-a-string structure of long telomeric DNAs under molecular crowding conditions. *J Am Chem Soc* 2012;**134**:20060–9. https://doi.org/10.1021/ja305384c
14. Frasson I, Pirota V, Richter SN *et al.* Multimeric G-quadruplexes: a review on their biological roles and targeting. *Int J Biol Macromol* 2022;**204**:89–102. https://doi.org/10.1016/j.ijbiomac.2022.01.197
15. Pirota V, Nadai M, Doria F *et al.* Naphthalene diimides as multimodal G-quadruplex-selective ligands. *Molecules* 2019;**24**:426.
16. Ahmed AA, Angell R, Oxenford S *et al.* Asymmetrically substituted quadruplex-binding naphthalene diimide showing potent activity in pancreatic cancer models. *ACS Med Chem Lett* 2020;**11**:1634–44.
17. Pirota V, Lunghi E, Benassi A *et al.* Selective binding and redox-activity on parallel G-quadruplexes by pegylated naphthalene diimide-copper complexes. *Molecules* 2021;**26**:5025.
18. Pérez-Soto M, Peñalver P, Street STG *et al.* Structure-activity relationship studies on divalent naphthalene diimide G quadruplex ligands with anticancer and antiparasitic activity. *Bioorg Med Chem* 2022;**71**:116946.
19. Pirota V, Platella C, Musumeci D *et al.* On the binding of naphthalene diimides to a human telomeric G-quadruplex multimer model. *Int J Biol Macromol* 2021;**166**:1320–34.
20. Platella C, Pirota V, Musumeci D *et al.* Trifunctionalized naphthalene diimides and dimeric analogues as G-quadruplex-targeting anticancer agents selected by affinity chromatography. *Int J Mol Sci* 2020;**21**:1964.
21. Doria F, Salvati E, Pompili L *et al.* Dyads of G-quadruplex ligands triggering DNA damage response and tumour cell growth inhibition at subnanomolar concentration. *Chemistry* 2019;**25**:11085–97.
22. Manoli F, Doria F, Colombo G *et al.* The binding pocket at the interface of multimeric telomere G-quadruplexes: myth or reality? *Chemistry* 2021;**27**:11707–20. https://doi.org/10.1002/chem.202101486
23. Licchelli M, Biroli AO, Poggi A *et al.* Excimer emission induced by metal ion coordination in 1,8-naphthalimide-tethered iminopyridine ligands. *Dalton Trans* 2003;**23**:4537–45. https://doi.org/10.1039/b308439f
24. Pirota V, Bisbano G, Serra M *et al.* cRGD-functionalized silk fibroin nanoparticles: a strategy for cancer treatment with a potent unselective naphthalene diimide derivative. *Cancers* 2023;**15**:1725. https://doi.org/10.3390/cancers15061725
25. Brynn Hibbert D, Thordarson P. The death of the Job plot, transparency, open science and online tools, uncertainty estimation methods and other developments in supramolecular chemistry data analysis. *Chem Commun* 2016;**52**:12792–805. https://doi.org/10.1039/C6CC03888C
26. Chen W, Hahn WC. SV40 early region oncoproteins and human cell transformation. *Histol Histopathol* 2003;**18**:541–50.
27. Zimmer J, Tacconi EMC, Folio C *et al.* Targeting BRCA1 and BRCA2 deficiencies with G-quadruplex-interacting compounds. *Mol Cell* 2016;**61**:449–60. https://doi.org/10.1016/j.molcel.2015.12.004
28. Iachettini S, Ciccarone F, Maresca C *et al.* The telomeric protein TERF2/TRF2 impairs HMGB1-driven autophagy. *Autophagy* 2023;**19**:1479–90. https://doi.org/10.1080/15548627.2022.2138687
29. Platella C, Gaglione R, Napolitano E *et al.* DNA binding mode analysis of a core-extended naphthalene diimide as a conformation-sensitive fluorescent probe of G-quadruplex structures. *Int J Mol Sci* 2021;**22**:10624. https://doi.org/10.3390/ijms221910624
30. Trott O, Olson AJ. AutoDock Vina: improving the speed and accuracy of docking with a new scoring function, efficient optimization, and multithreading. *J Comput Chem* 2010;**31**:455–61.
31. Horn HW, Swope WC, Pitera JW *et al.* Development of an improved four-site water model for biomolecular simulations: tIP4P-Ew. *J Chem Phys* 2004;**120**:9665–78. https://doi.org/10.1063/1.1683075
32. Pérez A, Luque FJ, Orozco M. Dynamics of B-DNA on the microsecond time scale. *J Am Chem Soc* 2007;**129**:14739–45. https://doi.org/10.1021/ja0753546
33. Dans PD, Danilāne L, Ivani I *et al.* Long-timescale dynamics of the Drew-Dickerson dodecamer. *Nucleic Acids Res* 2016;**44**:4052–66. https://doi.org/10.1093/nar/gkw264
34. Dans PD, Walther J, Gómez H *et al.* Multiscale simulation of DNA. *Curr Opin Struct Biol* 2016;**37**:29–45. https://doi.org/10.1016/j.sbi.2015.11.011
35. Ivani I, Dans PD, Noy A *et al.* Parmbsc1: a refined force field for DNA simulations. *Nat Methods* 2016;**13**:55–8. https://doi.org/10.1038/nmeth.3658
36. Wang J, Wolf RM, Caldwell JW *et al.* Development and testing of a general amber force field. *J Comput Chem* 2004;**25**:1157–74. https://doi.org/10.1002/jcc.20035
37. Joung IS, Cheatham TE 3rd. Determination of alkali and halide monovalent ion parameters for use in explicitly solvated biomolecular simulations. *J Phys Chem B* 2008;**112**:9020–41. https://doi.org/10.1021/jp8001614
38. Zivanovic S, Bayarri G, Colizzi F *et al.* Bioactive conformational ensemble server and database. A public framework to speed up *in silico* drug discovery. *J Chem Theory Comput* 2020;**16**:6586–97. https://doi.org/10.1021/acs.jctc.0c00305
39. Sousa da Silva AW, Vranken WF. ACPYPE—AnteChamber PYthon Parser interfacE. *BMC Res Notes* 2012;**5**:367. https://doi.org/10.1186/1756-0500-5-367
40. Castelli M, Serapian SA, Marchetti F *et al.* New perspectives in cancer drug development: computational advances with an eye to design. *RSC Med Chem* 2021;**12**:1491–1502. https://doi.org/10.1039/D1MD00192B
41. Norberg J, Nilsson L. Solvent influence on base stacking. *Biophys J* 1998;**74**:394–402. https://doi.org/10.1016/S0006-3495(98)77796-3
42. Rharbi Y, Winnik MA. Salt effects on solute exchange in sodium dodecyl sulfate micelles. *J Am Chem Soc* 2002;**124**:2082–3. https://doi.org/10.1021/ja0123397
43. Jana J, Mohr S, Vianney YM *et al.* Structural motifs and intramolecular interactions in non-canonical G-quadruplexes. *RSC Chem Biol* 2021;**2**:338–53. https://doi.org/10.1039/D0CB00211A
44. Petraccone L. Higher-order quadruplex structures. *Top Curr Chem* 2013;**330**:23–46. https://doi.org/10.1007/128_2012_350
45. Jaroszewski JW, Clausen V, Cohen JS *et al.* NMR investigations of duplex stability of phosphorothioate and phosphorodithioate

DNA analogues modified in both strands. *Nucleic Acids Res* 1996;**24**:829–34.
46. Thier SO. Potassium physiology. *Am J Med* 1986;**80**:3–7.
47. Doria F, Oppi A, Manoli F *et al.* A naphthalene diimide dyad for fluorescence switch-on detection of G-quadruplexes. *Chem Commun* 2015;**51**:9105–8. https://doi.org/10.1039/C5CC01536G
48. Del Villar-Guerra R, Trent JO, Chaires JB. G-quadruplex secondary structure obtained from circular dichroism spectroscopy. *Angew Chem Int Ed Engl* 2018;**57**:7171–5. https://doi.org/10.1002/anie.201709184
49. Greider CW, Blackburn EH. Identification of a specific telomere terminal transferase activity in *Tetrahymena* extracts. *Cell* 1985;**43**:405–13. https://doi.org/10.1016/0092-8674(85)90170-9
50. Bryan TM, Englezou A, Dalla-Pozza L *et al.* Evidence for an alternative mechanism for maintaining telomere length in human tumors and tumor-derived cell lines. *Nat Med* 1997;**3**:1271–4. https://doi.org/10.1038/nm1197-1271
51. Biffi G, Tannahill D, McCafferty J *et al.* Quantitative visualization of DNA G-quadruplex structures in human cells. *Nature Chem* 2013;**5**:182–6. https://doi.org/10.1038/nchem.1548
52. Kuo LJ, Yang LX. Gamma-H2AX—a novel biomarker for DNA double-strand breaks. *In Vivo* 2008;**22**:305–9.
53. Iachettini S, Biroccio A, Zizza P. Therapeutic use of G4-ligands in cancer: state-of-the-art and future perspectives. *Pharmaceuticals* 2024;**17**:771. https://doi.org/10.3390/ph17060771
54. Weiswald LB, Bellet D, Dangles-Marie V. Spherical cancer models in tumor biology. *Neoplasia* 2015;**17**:1–15. https://doi.org/10.1016/j.neo.2014.12.004

Received: June 17, 2024. **Revised:** March 26, 2025. **Editorial Decision:** March 27, 2025. **Accepted:** April 2, 2025